

The observable properties of cool winds from galaxies, AGN, and star clusters - II. Multiphase wind in M82

Yuxuan Yuan

A thesis submitted for the degree of
Bachelor of Philosophy with Honours in Astronomy
and Astrophysics
The Australian National University

August 2021

Draft Copy – 26 August 2021

© Yuxuan Yuan 2019

Except where otherwise indicated, this thesis is my own original work.

Yuxuan Yuan
26 August 2021

To my mum, who always listened to me and supported me when I was down.

Acknowledgments

First, I would like to thank my supervisors Prof. Mark Krumholz and Prof. Crystal Martin, who have given me valuable advice and guidance on the project during the honours year. I am especially thankful to Prof. Mark Krumholz for his support to me during my entire undergraduate degree. Without their experienced supervising and detailed comments on my draft, I would not make rapid progress on my thesis.

I next want to thank other Mark's research group members, including Dr. Piyush Sharda, Shyam Melon, Zefeng Li, Roland Crocker, Zipeng Hu, Donghee Nam, Matthew Sampson, for their fruitful suggestions and ideas on my thesis. I would like to thank Dr Ella Wang and Dr James Beattie who generously shared their well-written thesis to me, and Marcus Birch and Prof. Mike Ireland who gave me valuable advice on my final draft of the thesis.

Lastly, I would like to thank my parents, Yaling Xu and Yi Yuan, for always supporting me when I need accompany.

Abstract

Galactic winds have a large impact on galaxy formation and evolution, and recent high-resolution and sensitive observations of this phenomenon have given us unprecedented rich sets of data. We apply a novel analytical model to constrain the kinematics of a multi-phase outflow with spatially resolved, multi-wavelength observations in M82. Our model is fully characterised by parameters describing geometry and mass outflow rate, and physics prescriptions for the driving mechanism, gravitational potential and cloud expansion law. We apply this approach to two distinct cool phases of wind in M82, the cold molecular phase and the warm neutral phase, and compare their results systematically.

Our best-fitting model reproduces an edge-on orientation and bi-conical geometry for both phases, in line with earlier studies. The measured outflow rate of the warm neutral phase is larger than that of the cold molecular phase, but are both similar to the SFR at the order-of-magnitude level. Our fits further show that for both phases, the gas clouds are radiatively driven and maintain a constant cross-sectional area as they propagate out. Overall our model shows good agreement with the observations, both for the sample spectra used for the fits and for the full 2D moment maps.

Our results suggest a picture where strong magnetic fields in M82 thread the launched gas clouds and prevent them from expanding and subsequently being destroyed. The cold molecular outflow in M82 forms a galactic fountain within which the bulk of the mass falls back after travelling no higher than about 5 kpc above the galactic disc. Our modelling also shows that it is misleading to separate wind material from bound gas simply by imposing a hard velocity cutoff in observed spectra.

Contents

| | |
|---|------------|
| Acknowledgments | vii |
| Abstract | ix |
| 1 Introduction | 1 |
| 1.1 Theoretical understandings of galactic wind | 2 |
| 1.1.1 Physical nature | 3 |
| 1.1.2 How do galactic winds affect galaxy formation and evolution? . | 4 |
| 1.1.3 Limitations | 4 |
| 1.2 Previous Observational diagnostics | 5 |
| 1.2.1 Spectroscopy | 6 |
| 1.2.2 Extracting information from the observations | 6 |
| 1.3 Goal and outline of our thesis | 8 |
| 2 Methods | 9 |
| 2.1 Observations of Outflow in M82 | 9 |
| 2.1.1 Outflows in M82 | 11 |
| 2.2 Galactic wind line radiative transfer model | 11 |
| 2.2.1 Kinematic structure | 12 |
| 2.2.2 Geometry and mass flux | 14 |
| 2.2.3 Synthetic spectra | 15 |
| 2.2.4 Rotation | 16 |
| 2.3 Fitting method | 17 |
| 2.3.1 Parameter fitting | 17 |
| 2.3.2 Which combination of driving mechanism, potential and ex- pansion law? | 18 |
| 3 Results | 19 |
| 3.1 Model galaxy | 19 |
| 3.2 Warm neutral phase | 22 |
| 3.2.1 Best-fitting physical parameters | 22 |
| 3.2.2 Model validation | 22 |
| 3.2.3 Driving mechanism, potential and expansion law | 26 |
| 3.3 Cold molecular phase | 30 |
| 3.3.1 Best-fitting physical parameters | 30 |
| 3.3.2 Model validation | 33 |
| 3.3.3 Driving mechanism, potential and expansion law | 34 |

| | | |
|----------|---|-----------|
| 4 | Discussion | 35 |
| 4.1 | A physical picture of cool winds in M82 | 35 |
| 4.1.1 | Origin and evolution of cool gas clouds | 35 |
| 4.1.2 | Fountain scenario of M82 | 36 |
| 4.2 | Caveats | 38 |
| 5 | Conclusion | 41 |
| 5.1 | Summary | 41 |
| 5.2 | Future work | 42 |
| A | how to extend the model to include rotation in the outflow | 43 |
| A.1 | Coordinate transformations | 43 |
| A.2 | Effect on observables | 45 |

List of Figures

- 1.1 Density (upper panel) and temperature (bottom panel) slices through the x - z plane of the adiabatic nuclear outflow simulation of a model galaxy at 10, 25, 50, and 60 Myr. The high-resolution and three-dimensional nature of the simulation results in a high degree of structure in the outflow, which is particularly visible in the turbulent regions at later times. Credit: Schneider et al. [2018] 2
- 1.2 Examples of double-peaked emission-line profiles in the nebulae of M82, NGC253, NGC4945, Arp220, and IRAS00182-7112. The identifications of each components in this emission-line profiles are indicated by the following symbols: for IRAS 00182—7112, the [O III] $\lambda\lambda 4959, 5007$ lines are denoted by O' and O, respectively, while for the other five galaxies the [N II] $\lambda 6548$, H α , and [N II] $\lambda 6584$ lines are denoted by N', H, and N, respectively. In some cases, a blueshifted H component falls on top of a redshifted N' component or a redshifted H component falls on top of a blueshifted N component, and these are so indicated., credit: [Heckman et al., 1990]. 5
- 1.3 Normalised profiles of FUV absorption lines in cB58, from various neutral and low-ionisation elements that trace warm neutral phase outflow, credit: [Pettini et al., 2002]. 7
- 2.1 Velocity-integrated intensity (top row) and first and second moment maps (middle and bottom row) for the observations of the CO $2 \rightarrow 1$ [Leroy et al., 2015] (left) and H I 21 cm lines [Martini et al., 2018] (right). We have oriented our coordinates so that the major and minor axis of the galaxy defined in Martini et al. [2018] lie along the x and y axis, respectively. We have also shifted the velocity field to the systemic velocity of 211 km/s. The white region in the 21 cm map is masked because it is dominated by galaxy emission. We can clearly see the structure of evidence of a rotating disc in the midplane of the first moment map, as well as the outflow region off the disc plane. We select several spectra within a bicone with opening angle of 45 degrees within the outflow region ($y > 0.8$ kpc). The positions of the selected spectra aperture size over which they are averaged is shown by the orange squares. 10

-
- 3.1 Corner plot showing the 1D and 2D histograms of the posterior PDFs of the parameters ϕ , θ_{in} , θ_{out} , $\log \dot{M}$ and τ_0 of the warm neutral phase outflow, as determined by MCMC optimisation. Histograms show 1D marginal PDFs for each parameter; 2D maps show 2D probability densities. The model fit shown is for a radiatively-driven wind in a point gravitational potential, for clouds that maintain constant area as they flow outward; this combination of driving, potential, and cloud expansion yields the highest Akaike weight as compared to other combinations. 21
- 3.2 Predicted versus observed HI 21 cm spectra; each panel shows the spectrum at one of our sample positions, expressed as brightness temperature T_B as a function of velocity v , with $v = 0$ corresponding to the systemic velocity of M82. The lines shown are the predicted spectra adopting the value of parameters that gives the maximum value of likelihood function in MCMC (blue line), and using the parameters from 5 random walkers at the last iteration of MCMC sampling (orange lines). For comparison, we also show the observed spectrum with its 1σ error (grey region). 23
- 3.3 Same as Figure 3.2, but now showing how the predicted spectra vary in response to changes in the fit parameters. The best-fit case is shown by the blue line and the observed spectrum with 1σ errors is shown by the grey region, as in Figure 3.2, while spectra produced by varying ϕ , θ_{in} with θ_{out} , \dot{M} and τ_0 are shown in orange, green, red and purple, respectively. 24
- 3.4 Velocity-integrated intensity (top row) and brightness temperature weighted second moment map (bottom row) for the observations (left), theoretical predictions using our best-fitting model (middle) and the residual between the two (right) for HI 21 cm line. The black lines show our best-fitting angles θ_{in} and θ_{out} for the inner and outer angles of the outflow cone. The grey central region is a mask to block out 0.6 kpc around the galactic disc. 24
- 3.5 Same as Figure 3.2, but now showing how the predicted spectra vary in response to the choices of potential and expansion law, for radiatively driven winds. We show the best-fitting spectra for each individual combination of potential and expansion law. The spectrum produced with the combination that yields the highest Akaike weight is shown by the thickest line and the observed spectrum with 1σ errors is shown by the grey region, as in Figure 3.2. Spectra adopting point and isothermal gravitational potential are shown in solid and dashed lines, while those adopting constant area, intermediate, and constant solid angle expansion laws are shown in blue, yellow and red line, respectively. . . 27

| | | |
|------|---|----|
| 3.6 | Same as Figure 3.2, but now showing how the predicted spectra vary in response to the choices of driving mechanism, for point gravitational potential and constant area expansion. We show the best-fitted spectra for each individual driving mechanism. The spectra produced with the combination that yields the highest Akaike weight is shown by the thickest line and the observed spectrum with 1σ errors is shown by the grey region, as in Figure 3.2, while spectra adopting ideally, radiatively and hot gas driven wind are shown in blue, orange and green, respectively. | 28 |
| 3.7 | Same as figure 3.1, but show the results for CO. | 31 |
| 3.8 | Same as figure 3.2, but show the results for CO. | 31 |
| 3.9 | Same as figure 3.3, but show the results for CO. | 32 |
| 3.10 | Same as figure 3.4, but show the results for CO. | 32 |
| 3.11 | Same as figure 3.5, but show the results for CO. | 33 |
| 3.12 | Same as figure 3.6, but show the results for CO. | 34 |
| 4.1 | Molecular phase mass outflow rate as a function of radius. The blue line shows the total outflow rate whereas orange line shows the outflow rate only considering material moving faster than the escape velocity. | 37 |
| 4.2 | Fraction of the outflow material which moves faster than the escape speed as a function of radius. We see the acceleration processes increase the fraction of high velocity cloud at large radius of about 2 kpc. | 38 |

List of Tables

| | | |
|-----|--|----|
| 2.1 | Summary of the ingredients of KTOM17 model. The first five rows list the model prescriptions with their descriptions and choices, while the rest list the model parameters with their descriptions and ranges. | 15 |
| 3.1 | Best-fitting parameters and Akaike weights obtained for all combinations of driving mechanism (Column 1), potential (Column 2) and expansion law (Column 3) for the warm neutral phase outflow. We highlight the case that gives the highest Akaike weight. Values are specified in the form $p(50)_{p(16)-p(50)}^{p(84)-p(50)}$, where $p(q)$ is the q th percentile of the marginalised posterior PDF for that quantity. The first three Column 1: driving mechanism; Column 2: gravitational potential; Column 3: cloud expansion law; | 20 |
| 3.2 | Same as table 3.1, but show the results of fits for CO. | 30 |

Introduction

In 1963, Lynds and Sandage conducted the first observation of high velocity warm ionized outflow found in the central region of the starburst galaxy M82 [Lynds and Sandage, 1963] and discovered that the powerful explosion events of M82 drive the surrounding gas out to a velocity much larger than the local escape speed. This shows that galaxies are not ‘isolated islands’ as previously thought in the eighteenth century [Wright, 1750]. From then on, more and more subsequent observations on this phenomenon have been performed, which revealed that galactic winds are ubiquitous across nearly all starburst or active galactic nuclei (AGN) dominated galaxies at both low and high redshift [Veilleux et al., 2005; Heckman and Thompson, 2017; Veilleux et al., 2020], and there are multiple phases within them. The hot phase outflows, characterised by their high temperature ($\sim 10^8$ K) and high speed, are widely observed in X-ray emission around the nuclear region and carries most of the energy budget as long as strong outflows exist. Cool phase outflows ($\sim 10 - 10^4$ K), on the other hand, are much denser than the hot component and carry most of the mass.

It has been proven to be difficult, both observationally and theoretically, to study and interpret this ubiquitous phenomenon in galaxies. As a result, the study of outflows, particularly for their cool phase, is a particularly young area of research with a history of about 20 years. Some fundamental problems in this field that are still not fully resolved include:

1. Physical nature: How is the galactic wind triggered by Supernovae (SNe), radiation pressure or AGN? How is their strength dependent on galactic activities and properties?
2. Feedback effect: How will it affect galaxy formation and evolution? How will it regulate the life cycle of galaxies? Will the outflows carry mass, metals, momentum and energy out to intergalactic scale, or fall back to the host galaxies?
3. Observational constraints: How to distinguish the outflow from the galactic disc? How to extract information from multi-wavelength observations, such as the multiphase structure and driving mechanism?

In this chapter, I will give a review of the current understandings for the above three questions and introduce the goal in this thesis. Section 1.1 summarises the

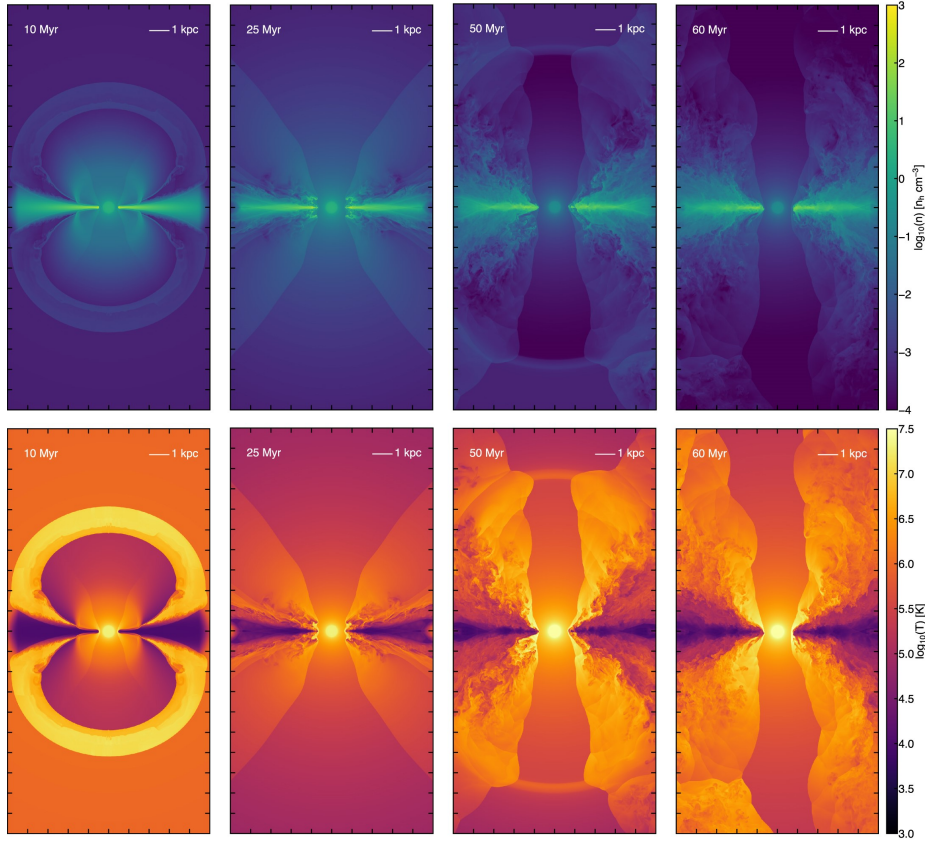


Figure 1.1: Density (upper panel) and temperature (bottom panel) slices through the x - z plane of the adiabatic nuclear outflow simulation of a model galaxy at 10, 25, 50, and 60 Myr. The high-resolution and three-dimensional nature of the simulation results in a high degree of structure in the outflow, which is particularly visible in the turbulent regions at later times. Credit: Schneider et al. [2018]

current theoretical understandings of galactic winds while Section 1.2 presents the common observational techniques used to extract information from the observations. In Section 1.3, we describe the goal and outline of the thesis.

1.1 Theoretical understandings of galactic wind

As the physics involved in galactic winds are intrinsically complex and multi-scale, theorists usually conduct detailed numerical simulation of this phenomenon in galactic scale [Hopkins et al., 2012; Smith et al., 2020] or cosmological scale [Nelson et al., 2019] to gain the most accurate results, with the cost of high calculation efficiency. The advantages of this kind of exercises have three folds. First, we create a direct channel to investigate the kinematic, thermal and chemical structures of the wind. Second, it can separate the effect of different physics governing the galactic wind by

enabling and disabling them. Third, we give a deeper interpretation to the observations by comparing synthetic observations to the real ones.

In this section we summarize our understandings of this phenomenon from recent theoretical studies, with particular focuses on its physical nature and how it affect galaxy formation and evolution.

1.1.1 Physical nature

The first widely accepted scenario for the galactic winds is proposed by Chevalier and Clegg [1985], which suggests that galactic wind is a result of supernovae (SNe) feedback. In this scenario, the explosion energy produced by SNe is partly thermalised into the surrounding hot plasma in the nuclei region of the galaxy. These hot plasma has a larger pressure than the surrounding medium and drives hot and fast outflow that then flows out of the nuclei region purely adiabatically and mass-conserving. This model gives a natural explanation of the origin of hot winds but can not explain the cool winds that are widely observed.

The theoretical models that can explain the cool winds only appear several decades later, including both numerical simulations and analytical models. However, these models indicate different physical origins and natures for the cool winds. In one scenario, Thompson et al. [2016] suggests that the central cool gas is rapidly shredded and shock heated into the hot winds near the nuclei region, this initial adiabatic hot outflows then undergo radiative cooling beyond a cooling radius of several kpc, resulting in the cool gas widely observed in circum-galactic medium (CGM) and intergalactic medium (IGM). However, numerical simulations conducted in Krumholz and Thompson [2013]; McCourt et al. [2015]; Schneider et al. [2018] argue that cool outflows have another origin. In this scenario, a large number of cool gas clouds are driven out of the galactic disc via the ram pressure of hot wind or radiation pressure from the central source. These cool gas clouds maintain their phase structure along the trajectories as opposed to Thompson et al. [2016], either because they are driven by some non-destructive mechanisms such as radiation pressure, or there are some protective mechanisms that prevent the clouds from shredding into the hot winds. We give one state-of-art example of this scenario in Figure 1.1, which shows the density and temperature structure of simulated outflow at 4 different times. We see that the hot gas flows through the central axis, with cool wind surrounding it. However, whether these cold phase clouds could really survive through the hot gas outflow, i.e. the ‘cloud crushing’ problem, is highly debated and requires detailed numerical simulations of the turbulent mixing layers between fast-moving hot and cool fluid [Ji et al., 2019; Fielding et al., 2020; Tan et al., 2020; Scannapieco and Brüggen, 2015; Zhang et al., 2017; Banda-Barragán et al., 2019; Gronke and Oh, 2018, 2020; Li et al., 2020; Cottle et al., 2020].

1.1.2 How do galactic winds affect galaxy formation and evolution?

The galactic winds have a significant impact on the life-cycle of galaxies and universe at nearly all dynamical scales, from the giant molecular clouds (GMC) and the interstellar medium (ISM) within the galaxy (~ 1 pc), to galactic properties (~ 10 kpc) or even cosmological large scale structure (~ 1 Mpc).

At GMC scales, SNe feedback is the dominant energy source of turbulence in the surrounding ISM for low redshift galaxies [Krumholz and Burkhardt, 2016; Krumholz et al., 2018; Bacchini et al., 2020; Gallegos-Garcia et al., 2020]. Ultraviolet (UV) radiation from young stellar cluster exerts radiation pressure on dust grains that are kinetically coupled to gas, locally disrupting the giant molecular cloud (GMC) and expelling the dense gas out to a high speed [Kim et al., 2018]. Galactic winds driven by individual or clustered SNe could exhaust the molecular gas content and quench the star formation in the galactic nuclei within tens of million years, making it the dominant mechanism to explain low star formation efficiency typically observed in nearly all galaxies [Hopkins et al., 2011].

At galactic scales, galactic winds affect the life-cycle of the entire galaxy, and regulate the balance between star formation, inflow and outflow, which offer a solution for the long-standing ‘over-cooling’ problem. Without galactic winds, gas just constantly flows into the gravitational potential well of the dark matter halo and gives a much higher star formation rate than observed [Springel and Hernquist, 2003]. Feedback regulates star formation at the galactic scales, provides support against gravity and therefore maintains the marginal equilibrium of the entire galactic disc [Murray et al., 2005; Thompson et al., 2005]. It also suppresses the total stellar mass and baryonic budget of the galaxy, and shapes the stellar mass-halo mass relation [Hopkins et al., 2014].

At cosmological scales, the escaped winds can entrain mass, metal and dust in the ISM and nucleosynthetic products in supernova ejecta to the circumgalactic medium (CGM) or even intergalactic medium (IGM) outside the galaxies [Nelson et al., 2018; Tumlinson et al., 2011; Muratov et al., 2017], making the IGM the largest reservoir of baryons and metals across the universe [Oppenheimer and Davé, 2006]. This provides a possible solution to a long-standing problem that baryonic mass fraction inside the dark matter halos is less than what it should be with cosmological parameters, which is referred as the ‘missing baryon problem’. However, some of the mass may form a galactic fountain and recycle back to the galaxies and trigger another cycle of star-forming activities [Bregman, 1980; Melioli et al., 2015; Marasco and Fraternali, 2017; Werk et al., 2019; Li and Tonnesen, 2020].

1.1.3 Limitations

We finish this section by noting a number of problems these simulations inevitably suffer. Both galactic scales and cosmological simulations cannot resolve all the physical scale involved in galactic winds, and adopt several subgrid models as a compromise. These subgrid models usually adopt several ad hoc parameters and tune them to match some of the observed scaling relations of galaxies [Springel and Hernquist,

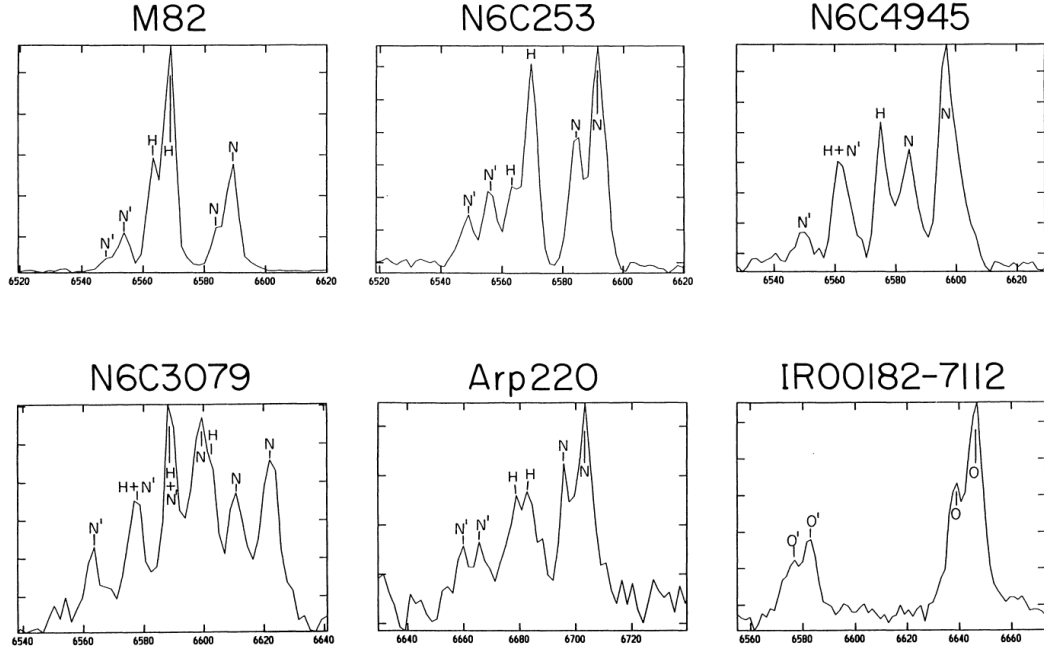


Figure 1.2: Examples of double-peaked emission-line profiles in the nebulae of M82, NGC253, NGC4945, Arp220, and IRAS00182–7112. The identifications of each component in this emission-line profiles are indicated by the following symbols: for IRAS 00182—7112, the $[\text{O III}] \lambda\lambda 4959, 5007$ lines are denoted by O' and O , respectively, while for the other five galaxies the $[\text{N II}] \lambda 6548$, $\text{H}\alpha$, and $[\text{N II}] \lambda 6584$ lines are denoted by N' , H , and N , respectively. In some cases, a blueshifted H component falls on top of a redshifted N' component or a redshifted H component falls on top of a blueshifted N component, and these are so indicated., credit: [Heckman et al., 1990].

2003]. This artificial adjustment, however, inevitably limits the self-consistency and predictive power of the model. Furthermore, even if numerical simulations provide the most accurate results, they are localized in a limited portion of parameter space. This makes them unreliable to extract information from the observations that are ‘sampled’ from a much larger portion of parameter space.

1.2 Previous Observational diagnostics

Apart from the above theoretical studies, another way to study the galactic wind is to extract information of kinematic and thermodynamic structure from observations. However, these kinds of measurements are non-trivial, both in the way we conduct such observations, and in the way we extract the information.

The first complication originates from the confusion of gas from winds and discs. In a real galaxy, the cool winds often spatially overlap with denser cool gas from the wind launching region, and hence are hard to distinguish with the imaging

technique. The way to resolve this is to rely on emission line and absorption line spectroscopy, which distinguish cool phase outflow based on velocity. The confusion can be mitigated even further by observing the off-plane outflow that is not polluted by the central gas from edge-on galaxies [Leroy et al., 2015]. We will describe these techniques and what we get from the observations in Section 1.2.1.

The second complication is about how to transform the observable to the underlying physical structure of the galactic wind. For this purpose, we usually rely on semi-analytical models that are capable of generating synthetic observations with a high computational efficiency, well suitable for constraining the model parameters from the observation and gaining physical insights. We will describe previous efforts in this direction in Section 1.2.2.

1.2.1 Spectroscopy

We first describe the emission line spectroscopy. Figure 1.2 shows us the double-peaked emission line spectra from six galaxies, which reveals the bi-conical geometry of the wind with cold gas sheath surrounding the central hot outflow [Heckman et al., 1990]. From emission line imaging, we can extract column density, velocity and mass outflow rate based on the conversion between mass and light [Leroy et al., 2015]. For cold molecular phase winds traced by optically thick line CO as an example, we usually adopt a constant conversion factor of $\alpha_{\text{CO}} = \Sigma_g / W_{\text{CO}} = 1 M_{\odot} (\text{K km s}^{-1} \text{pc}^2)^{-1}$ [Alatalo et al., 2011; Genzel et al., 2011; Janssen et al., 2016].

Although The emission line surveys provide detailed information of the spatial and kinematic distribution of gas, detecting emission lines in the outflow suffers more difficulties than the absorption lines. Even the most bright emission lines, including CO transition lines and H I 21cm line, have only been detected in a few local galaxies. As a result, detecting outflow in more distant galaxies usually relies on absorption lines of various species which probe a range of phases [Heckman et al., 2000; Martin, 2005; Rupke et al., 2005a,b; Steidel et al., 2010; Werk et al., 2014]. Such absorption line surveys usually carry rich spectroscopic information but limited spatial information, as they are intrinsically limited by the availability of the background sources. Observers usually select quasars as the background sources or view galaxies themselves as the source (detect absorption lines ‘down-the-barrel’). Figure 1.3 presents the absorption line profiles of several neutral and low ionisation elements taken from Pettini et al. [2002]. We see that the strongest transitions are characterised by broad line wings at velocity ranges of $\sim 1000 \text{ km/s}$, which indicates strong warm neutral phase outflow .

1.2.2 Extracting information from the observations

Beyond above direct extraction of information of density and velocity structure, a more complete picture of galactic wind can only be obtained via applying semi-analytical line transfer (SALT) model to the observations. For example, Steidel et al. [2010]; Prochaska et al. [2011] explain the stacked absorption profiles of ISM and

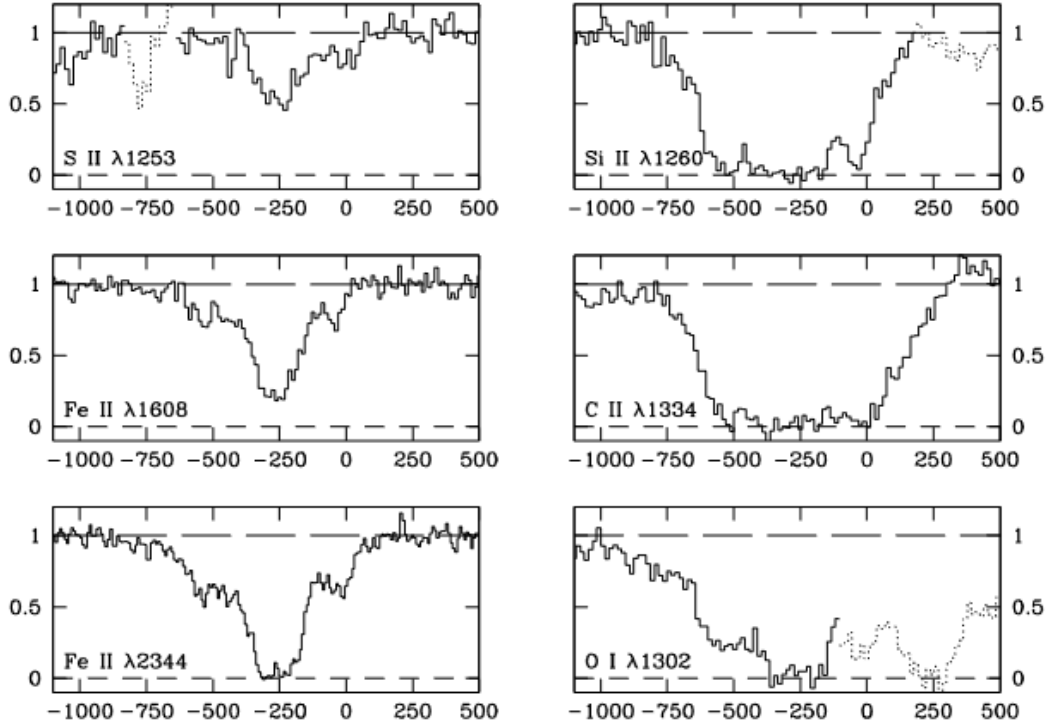


Figure 1.3: Normalised profiles of FUV absorption lines in cB58, from various neutral and low-ionisation elements that trace warm neutral phase outflow, credit: [Pettini et al., 2002].

CGM of hundreds of Lyman break galaxies (LBG) via a picture where these LBGs are partially covered by an ensemble of high-velocity optically thick clouds ($\tau > 1$). Lochhaas et al. [2018] shows that galactic wind-driven, radiatively cooling, expanding bubbles can explain the CGM properties observed with COS-Halo survey.

However, SALT models often adopt simplified or heuristic prescriptions to avoid the computational cost. For example, Models in Steidel et al. [2010]; Prochaska et al. [2011]; Scarlata and Panagia [2015]; Lochhaas et al. [2018] describe the wind as a fully-filled spherically symmetric expanding shell, and adopt density, velocity and covering fraction only as a simple function of radius from the center. A more realistic description of biconical geometry is adopted in [Carr et al., 2018], but it still can not fully describe the scenario that cold wind form a sheath surrounding the cone of central hot outflow, and it still uses the simplified kinematic structure inherited from Scarlata and Panagia [2015]. Although these models are able to roughly reproduce the stacked spectra, this diagnostics inevitably throw out much of the information hidden within individual un-stacked spectrum. Moreover, these models solely focus on a single phase of galactic wind, and hence can not get a unified picture of multi-phase outflow under one framework. Both of these problems raise great challenges for modern observational studies of galactic winds.

1.3 Goal and outline of our thesis

With the rapid development of modern observations of galactic winds, which are increasing in both resolution and precision, there is a clear need for models capable of describing spatially resolved multi-wavelength data. For this purpose, Krumholz et al. [2017b, hereafter KTOM17] proposed a semi-analytical model that gives a reasonable balance between physical complexity and numerical efficiency. The KTOM17 model can generate spatially resolved synthetic spectra based on a physical model for wind acceleration that depends on a few physical parameters and prescriptions, suitable for comparison to the resolved observations of wind. This model is implemented as an extension of the open-source code *Derive the Energetics and SPectra of Optically Thick Interstellar Clouds* (DESPOTIC) [Krumholz, 2014].

The goal of this thesis is to test the robustness of the model in confrontation with the real observational data. Specifically, we will apply the model to constrain the physical properties of the cool winds from the observations of multi-phase outflows in the dwarf starburst galaxy M82. We aim to extract much more detailed information about the properties of the wind than would have been possible with previous methods. The work presented in this thesis is the first spectrum-by-spectrum fitting for one of the most well-observed galactic winds. Furthermore, this is also the first joint study of multiple phases of the wind (atomic and molecular gas) under one theoretical framework, which enables us to explore the relationship between the phases.

The structure of the thesis is as follows: In Chapter 2, we describe the KTOM17 model, the data to which we will apply it, and the methods we use to fit to the observed data. We then present the results from measurements in Chapter 3. We next discuss our results in Chapter 4 and finally summarise our conclusions in Chapter 5.

Methods

As observations of galactic winds have reached higher spatial and spectroscopic resolutions, it has become important to extract the rich information hidden within them. However, inferring this information is non-trivial and requires detailed physical modelling and accurate statistical tools. In order to conduct this exercise, we present our state-of-the-art model, including a large set of parametrised and prescribed physical properties of winds. We aim to constrain these parameters and prescriptions and investigate which features of observed, spatially-resolved spectra carry information about which physical parameters. In this chapter, we describe the methods by which we infer the physics of winds from observations in detail. We introduce the observational data to which we compare and their properties in Section 2.1. In Section 2.2 we summarise the nature and the detailed prescriptions in our model and how they affect the generated spectrum. We describe our approach to fit multiple parameters to the observational data and compare different combinations of model choices in Section 2.3. The source code and data used in this thesis are available from <https://github.com/yyx319/multiphase-outflow-M82>.

2.1 Observations of Outflow in M82

This section presents the observations of outflow in Messier 82 (M82), which is one of the most well-studied cases in this field. We first give a general overview of M82. M82 is a typical edge-on (with an inclination angle $\sim 80^\circ$), starburst galaxy [O’Connell and Mangano, 1978; O’Connell et al., 1995], located only 3.6 Mpc away ($1 \text{ arcsec} \sim 17.5 \text{ pc}$) [Freedman et al., 1994], making it a promising candidate for the study of outflow around the minor axis. Hubble Space Telescope (HST) imaging revealed that M82 hosts very young massive clusters, concentrated in its central 500 pc (30 arcsec) nucleus. M82 is characterised by its intense star-bursting activities, and is often referred to as the ‘Cigar Galaxy’. The star-bursting events in M82 are commonly thought to be merger-driven and triggered by a tidal interaction with neighbouring galaxy M81.

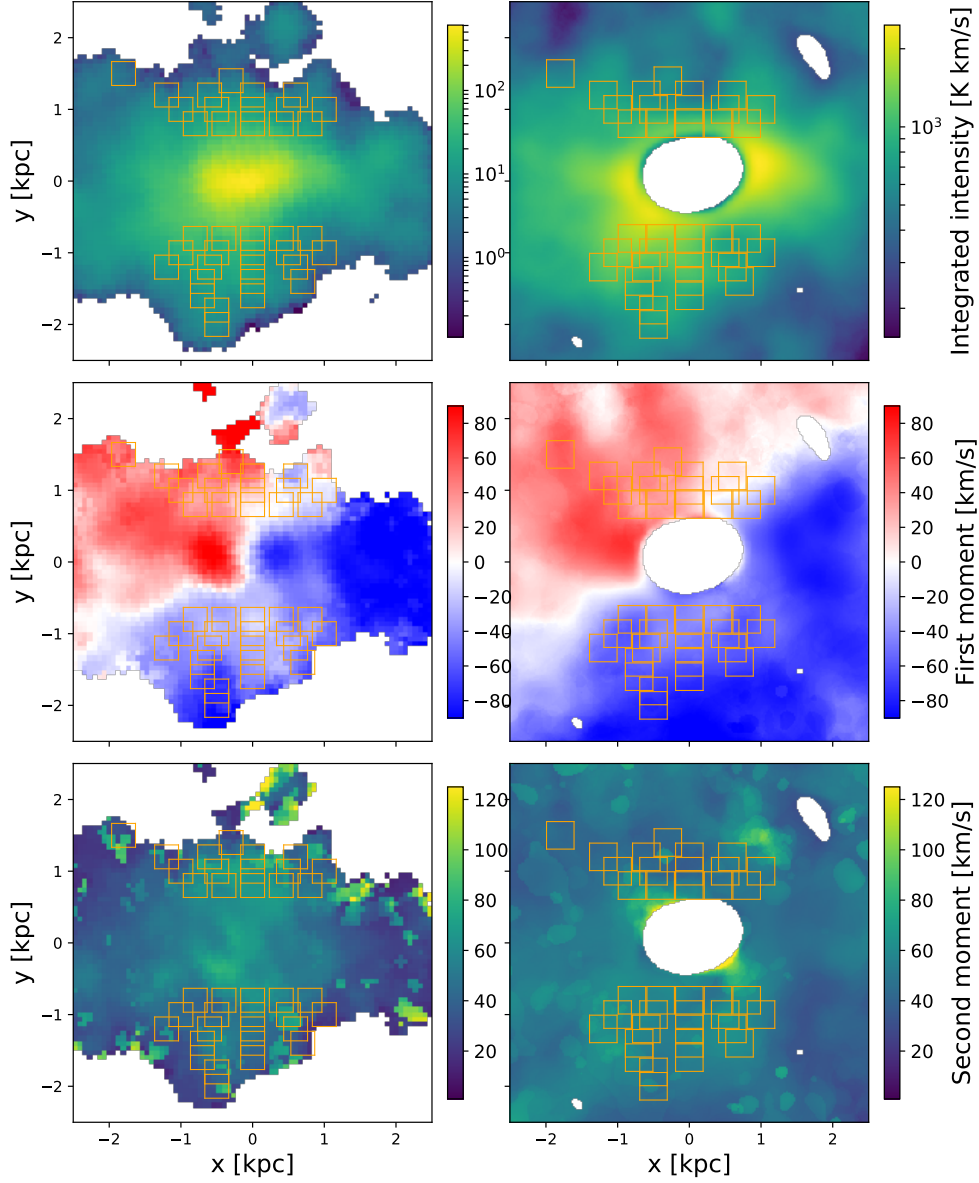


Figure 2.1: Velocity-integrated intensity (top row) and first and second moment maps (middle and bottom row) for the observations of the CO 2 \rightarrow 1 [Leroy et al., 2015] (left) and H I 21 cm lines [Martini et al., 2018] (right). We have oriented our coordinates so that the major and minor axis of the galaxy defined in Martini et al. [2018] lie along the x and y axis, respectively. We have also shifted the velocity field to the systemic velocity of 211 km/s. The white region in the 21 cm map is masked because it is dominated by galaxy emission. We can clearly see the structure of evidence of a rotating disc in the midplane of the first moment map, as well as the outflow region off the disc plane. We select several spectra within a bicone with opening angle of 45 degrees within the outflow region ($y > 0.8$ kpc). The positions of the selected spectra aperture size over which they are averaged is shown by the orange squares.

2.1.1 Outflows in M82

Various phases of winds from M82 has been observed and studied across the spectrum, from a hot phase observed in soft X-rays ($\sim 10^7$ K) [Watson et al., 1984; Bregman et al., 1995; Strickland et al., 1997; Lopez et al., 2020], to warm ionised gas associated with $H\alpha$ ($\sim 10^4$ K) [McKeith et al., 1995; Martin, 1998; Westmoquette et al., 2009], to a cool neutral phase seen in $H\text{I}$ 21cm (~ 5000 K) [Martini et al., 2018] to a cold molecular phase ($\lesssim 100$ K) [Leroy et al., 2015; Walter et al., 2002]. These recent observations support a picture that cool material traced by $H\text{I}$ and CO confine the central hot outflow, but will ultimately stall out or fall back as a fountain, while $H\alpha$ is associated with the interface between the hot outflow and surrounding cold gas.

In this thesis, we will focus on the cool phase outflow traced by CO and $H\text{I}$ in particular, and leave the warm ionised phase traced by $H\alpha$ for future work. To show the overall kinematic structure of the cool wind, we plot the velocity integrated intensity and first and second moment maps of the CO $J=2\rightarrow 1$ (Left) and $H\text{I}$ 21cm (Right) lines in Figure 2.1. We have oriented our coordinates so that the major and minor axis of the galaxy defined in Martini et al. [2018] lie along the x and y axis, respectively. We have also shifted the velocity field to the systemic velocity of 211 km/s. The white region in the 21 cm map is masked because it is dominated by galaxy emission. From the first moment map, we clearly see the structure of a rotating disc at the midplane, as well as the outflow region off the disc plane. We also see that $H\text{I}$ outflow is much more extended than the molecular outflow, which suggests they have different spatial distributions and mass outflow rates, which we will compare and discuss in the next chapter.

We next select the representative spectra to which we will compare our model. The principle of the selection is that the regions we pick should generally capture the rich information in the observation as a whole, so that our fitting is not overly biased to ‘small scale’ spectroscopic features at certain positions, and gives a reasonable fit to the entire observation. In accord with this principle, we extract spectra at a broad range of positions within a conical region with an opening angle of 45 degrees around the minor axis of the disc, above a height of 0.8 kpc ($y > 0.8$ kpc) so that we observe off-plane. To increase the signal to noise ratio, we stack the spectra within a square aperture with a size of $\pm 10''$ at each position, using the same positions in the CO and $H\text{I}$ maps. We show the positions of the selected spectra with their aperture size in Figure 2.1. Finally, we note that as the wind from M82 is asymmetric [Shopbell and Bland-Hawthorn, 1998], we will fit the model for the northern and southern parts of the outflow separately.

2.2 Galactic wind line radiative transfer model

We summarise the general features of our KTOM17 wind model in this section. We first describe how we model the kinematic structure in Section 2.2.1. Then we illustrate how to couple the bi-conical geometry and mass-outflow rate into our model in Section 2.2.2. We finally show our model’s capacity to generate the synthetic spectra

in Section 2.2.3.

2.2.1 Kinematic structure

KTOM17 adopt the wind-launching model described in Thompson and Krumholz [2016, hereafter TK16]. TK16 model the gas clouds in the galactic disc from which the wind is launched as an isothermal, turbulent fluid, which has a log-normal density probability density function (PDF) with a mean surface density of $\bar{\Sigma}_0$ at scale r_0 . The gas clouds are momentum-driven by some form of feedback mechanism, which supplies a constant momentum injection rate of \dot{p} per unit solid angle, driving mass out of the gravitational potential well. We define the generalised Eddington ratio Γ , as the ratio of the driving force to the gravitational force from regions with the mean surface density $\bar{\Sigma}_0$. We note that the non-uniform density distribution of ISM has an important implication for wind launching, as in this case even if $\Gamma < 1$, winds can still be produced by ejecting the lower tail of the gas column density PDF. In this scenario, the gas clouds with logarithmic column density $x = \ln \Sigma / \bar{\Sigma}_0$ that are below the critical value $x < x_{\text{crit}} = \ln \Gamma$ will be driven out. This is consistent with the idea that the outflows escape along the path of least resistance, as many previous numerical simulations revealed [Costa et al., 2014, 2015; Nelson et al., 2019]. KTOM17 extend the original model, combine it with the elements from Thompson et al. [2015] and Krumholz et al. [2017a], and compute the velocity and density structure, assuming that wind properties are only a function of radius from the galactic centre, and that the wind is time-steady.

We now give an overview of the derivation and the key elements and prescriptions within our model. We consider a cloud being driven out by some feedback mechanism from a galaxy with a specified gravitational potential, with the cloud's cross-sectional area to the driving force changing as it travels. We first assume a constant momentum deposition rate \dot{p} at the origin for ideally momentum-driven wind. This assumption is not valid in realistic cases as the momentum deposition rate depends on the physical process responsible for driving the wind, but it serves as a useful starting point before building more complex models. The total mass (from galaxy and dark matter halo) enclosed within radius r is M_r . The equation of motion for a cloud with a column density Σ_c and velocity v_r at radius r is then

$$\frac{dv_r}{dt} = v_r \frac{dv_r}{dr} = -\frac{GM_r}{r^2} + \frac{\dot{p}}{4\pi r^2 \Sigma_c} \quad (2.1)$$

We next non-dimensionalize the system by introducing the dimensionless radius, $a = r/r_0$, velocity $u_a = u/v_0$ (where $v_0 = \sqrt{GM_r(r_0)/r_0}$), and column density $x = \ln(\Sigma_{0,c}/\bar{\Sigma}_0)$. The solution to Equation (2.1) depends on the functional form of M_r and Σ_c on radius. We model the mass distribution $M_r = mM_0$, where $M_0 \equiv M_r(r_0)$, which determines the gravitational potential, with two choices: a point mass profile, $m = 1$, or an isothermal profile, $m = a$. We next model the evolution of the cloud's cross-sectional area to the driving forces as it moves outward, which we refer to as expansion law. We parametrise this process by introducing a function y such that the

surface density decreases as $\Sigma_c = \Sigma_{0,c}/y$, or, equivalently, the cloud area increases proportional to y . In extreme, the cloud may maintain a constant area, $y = 1$, or a constant solid angle, $y = a^2$. We also include an intermediate case, $y = a$, in between these extremes. With the above definitions, we can rewrite Equation (2.1) as

$$2u_a \frac{du_a}{da} = \frac{1}{a^2} (y\Gamma e^{-x} - m) \quad (2.2)$$

where $\Gamma = \dot{p}/4\pi GM_0 \bar{\Sigma}_0$ is the Eddington ratio. The first term on the RHS represents the driving forces exerted on the cloud, and scales with radius a as $1/a^2$ for constant area expansion, as $1/a$ for intermediate case, and as constant for constant solid angle case. The second term represents gravity, and scales with radius as $1/a^2$ for a point gravitational potential, and as $1/a$ for an isothermal gravitational potential. This equation can be solved analytically for u_a for each of our possible combinations of y and m , thereby giving the velocity of a cloud with initial log density x as a function of radius a ; refer to the Table 1 in KTOM17 that gives the solutions. This is the fundamental object we will use below to compute spectra, because combining the u_a curve with the distribution of column densities x in the launching region lets us know how much material there is moving at any given velocity at any given point in the wind.

In above calculation, we assume an idealised wind with a constant \dot{p} , which will certainly break down when the clouds reach a high velocity or a low surface density. For this reason, we introduce two potentially important and more realistic driving mechanisms. One is momentum injection from starlight, in the form of radiation pressure exerted on dust grains [Krumholz and Thompson, 2013; Costa et al., 2018; Zhang et al., 2018]. The dust grains then deposit the momentum they acquire into the surrounding collisionally-coupled gas and drive the wind. We parametrise this effect using a single extra parameter $\tau_0 = \kappa_F \bar{\Sigma}_0$, where κ_F is the flux-mean specific opacity of the dusty gas to starlight; the parameter τ_0 is the flux-mean optical depth at the mean surface density. The rate of momentum injection into a cloud is multiplied by a factor of $1 - e^{-\tau_0 \Sigma_c / \bar{\Sigma}_0}$ compared to ideal case, so that when the cloud is optically thick it receives the same momentum as in the ideal case, but as its dust optical depth declines, the momentum it receives diminishes because more and more of the starlight passes through it without being absorbed. The non-dimensional equation of motion in this case is

$$2u_a \frac{du_a}{da} = \frac{1}{a^2} \left\{ y\Gamma e^{-x} \left[1 - \exp \left(-\frac{e^x \tau_0}{y} \right) \right] - m \right\} \quad (2.3)$$

This equation, like Equation 2.2, is also analytically soluble for our various combinations of y and m ; refer to the Table 2 in KTOM17 that gives the solutions..

Another important driving mechanism is ram pressure from supernova heated gas. The mechanisms by which cool clouds are entrained by hot outflows are physically complicated and still not fully understood. However, we will just simplify this scenario by ignoring the destruction of clouds and introducing a free parameter describing the hot gas (dimensionless) velocity u_h . In this case the driving force de-

depends on the velocity contrast between the entrained cool clouds and hot gas. The rate of momentum injection into a cloud will be multiplied by a factor of $(1 - u_a/u_h)^2$ compared to ideal case, so the cloud receives less momentum as its radial velocity u_a approaches the hot gas velocity u_h . The non-dimensional equation of motion for this case then becomes

$$2u_a \frac{du_a}{da} = \frac{1}{a^2} \left[\Gamma y e^{-x} \left(1 - \frac{u_a}{u_h} \right)^2 - m \right] \quad (2.4)$$

This equation, although can not be solved analytically, can be computed numerically very straightforwardly, and we have precalculated the tabulated solutions to allow quick interpolation, for our various combinations of y and m .

In sum, the velocity structure of the wind in our model is determined by the driving mechanism, potential and expansion law. We list all these prescriptions with their choices in Table 2.1. Before proceeding further, we pause to point out that our solutions can be broken into two classes: some combinations will give rise to wind solutions, where all launched clouds always have net outward acceleration and thus escape to infinity, while others will give fountain solutions, where clouds stall at some radius and ultimately fall back. Consulting Equation (2.2), we see that which behaviour occurs depends on the competition between gravity and driving forces. In wind solutions, the clouds expand faster than the potential increases, $y > m$, so the launched clouds are constantly accelerated and reach infinity, while for fountain solutions $y < m$, even though clouds are accelerated initially, gravity will overweigh the driving force at large radii, so clouds will ultimately fall back. At the transition between wind and fountain solutions $y = m$, clouds with surface densities just below the critical value will move out at a near-zero velocity in our model under near-balance between gravity and driving forces. We will see below that wind and fountain solutions can produce distinct features in observed spectra, which we will exploit to distinguish between them.

2.2.2 Geometry and mass flux

In the above section, we have described an isotropic spherical wind. However, observed galactic winds [e.g., Shopbell and Bland-Hawthorn, 1998] are often biconical along the minor axis, as the outflows are usually blocked by the dense gas within the galactic disc. For this reason, we consider winds with a “cone sheath” geometry confined by two cones with outer opening angle $\theta_{\text{out}} \in (0, \pi/2]$ and inner opening angle $\theta_{\text{in}} \in [0, \theta_{\text{in}})$. The central axis of this cone has an inclination angle of $\phi \in (-\pi/2, \pi/2)$ relative to the plane of sky, where $\phi = 0$ corresponds to the central axis of the outflow cone lying exactly in the plane of the sky.

The parameter we next introduce is the isotropic mass outflow rate that describes the wind’s strength. This is related to the generalised Eddington ratio Γ that enters into our model. [Thompson and Krumholz, 2016] show that the mass outflow rate is

| Parameter & Prescriptions | Units | Description | Choices & range |
|---------------------------|---------------------------------|---|--|
| Driving mechanism | - | Physical process that deposits momentum into the surrounding material | ideal, radiation and hot gas |
| Potential | - | Mass distribution of galaxy and dark matter halo | point, isothermal |
| Expansion law | - | Dependence of cross sectional area to the driving force on the radius | constant area, intermediate and constant solid angle |
| τ_0 | - | Optical depth at mean surface density, only needed in radiatively driven wind | - |
| u_h | 170 km s ⁻¹ | Velocity of hot gas outflow, only needed in hot gas driven model | - |
| ϕ | - | Orientation angle of the outflow | $(-\pi/2, \pi/2)$ |
| θ_{in} | - | Inner opening angle of cone sheath | $[0, \pi/2)$ |
| θ_{out} | - | outer opening angle of cone sheath | $(\theta_{\text{in}}, \pi/2)$ |
| $\log \dot{M}$ | M _⊙ yr ⁻¹ | isotropic mass outflow rate of a particular phase outflow | $(-1, 3)$ |

Table 2.1: Summary of the ingredients of KTOM17 model. The first five rows list the model prescriptions with their descriptions and choices, while the rest list the model parameters with their descriptions and ranges.

related to the fraction of mass with column density below the critical value ζ_M via

$$\eta = \frac{f_A \dot{M}}{\dot{M}_*} = \frac{\zeta_M}{\epsilon_{\text{ff}}} \quad (2.5)$$

where $\epsilon_{\text{ff}} \approx 0.01$ as the star formation efficiency per free-fall time, \dot{M}_* is the star formation rate of the galaxy and $f_A = \cos \theta_{\text{in}} - \cos \theta_{\text{out}}$ is the covering fraction of the bi-conical outflow. We next write out the relation between ζ_M , Γ , and \mathcal{M} . The ζ_m is given by

$$\zeta_M = \frac{1}{2} \left[1 - \text{erf} \left(\frac{-2x_{\text{crit}} + \sigma_x^2}{2\sqrt{2}\sigma_x} \right) \right] \quad (2.6)$$

where the critical density is $x_{\text{crit}} = \ln \Gamma$ and the dispersion of log-normal distribution σ_x is

$$\begin{aligned} \sigma_x &= \sqrt{\ln(1 + R\mathcal{M}^2/4)}, \\ R &= \frac{1}{2} \left(\frac{3 - \alpha}{2 - \alpha} \right) \left[\frac{1 - \mathcal{M}^{2(2-\alpha)}}{1 - \mathcal{M}^{2(3-\alpha)}} \right], \\ \alpha &= 2.5 \end{aligned} \quad (2.7)$$

As ζ_M is a function of Γ and \mathcal{M} , we can then inversely solve for Γ from any value of ζ_M . The physical interpretation for this conversion is that a higher mass outflow rate implicates a larger proportion of clouds being driven out as a result of higher Eddington ratio, and hence affects the overall density structure of winds.

2.2.3 Synthetic spectra

In the above sections we have described the kinematic and geometric structure of bi-conical winds, and in this section we discuss the capability of our model to gener-

ate synthetic spectra from the underlying winds. In general cases, this requires full treatment of calculating emissivity as a complex function of density and temperature, and the radiative-transfer effects on the level population of species, which requires complex numerical calculation and is too expensive for parameter studies. For this reason, we consider two limiting cases for which the emissivity can be calculated analytically. The first is for the species in Local Thermal Equilibrium (LTE) with critical density much less than the mean density in the wind, like CO and H I 21 cm line. The second is for the subcritical lines with critical density far beyond the mean density in the wind, and negligible radiative trapping effect, including H α and CII 158 μ m lines. We include one another simple prescription that affects the modeling of radiative transfer effects, that is, whether the wind is correlated or uncorrelated. The key distinction between them is that whether individual clouds launched into the outflow are opaque (correlated) or transparent (uncorrelated), that is, are we dealing with a mist of water droplets where you can see through each individual droplet even if the mist as a whole opaque, or are we dealing with a cloud of dust where every individual dust grain in the air is itself opaque. For example, CO belongs to the correlated case, as it is an intrinsically much stronger line, and the typical cloud of CO emission is very optically thick, with typical value of $\tau \sim 50 - 100$. H I, on the other hand, belongs to the uncorrelated case, as the line is intrinsically very weak, and we expect it to be optically thin. With above modeling of emissivity and radiative transfer effects specified, DESPOTIC can analytically calculate the emission line profiles up to a single numerical integral, which allows fast evaluation and parameter studies.

2.2.4 Rotation

We end this section by noting that our model ignored the rotations of the outflows, which is potentially important for interpreting observations. As [Greve, 2004] pointed out, the outflow material entrains the rotation of the disc, although with a smaller value than that of disc. As a consequence, the spectra will be red-shifted in the west of the minor axis and blue-shifted in the east, which is what we observe in the first moment map in Figure 2.1. This asymmetry is not predicted by our model, as we only consider the motion of gas in radial rather than azimuthal direction.

In this thesis we add an ‘empirical’ implementation of rotation to our model. At each sky position of selected spectrum, we induce an artificial velocity shift to the synthetic spectrum (translate the profile along the velocity axis) to minimise the difference between model and data. And as a result they will have similar systematic velocity. This implementation, however, does not naturally model the underlying rotation structure of the wind and we leave a more physical and self-consistent rotation module for future work.

2.3 Fitting method

We next outline our strategy for fitting the model to the data. We consider a series of wind models described by all combinations of driving mechanism, potential and expansion law. For each combination, we optimise the set of physical parameters under a Bayesian framework. We then identify the combination that gives the best fit between model and data.

2.3.1 Parameter fitting

We fit four parameters, ϕ , θ_{in} , θ_{out} , and \dot{M} , for ideal momentum driven winds, with an additional parameter τ_0 for radiation driven and u_h for hot gas driven winds, respectively. We adopt uniform priors for $\sin(\phi)$ ($\phi \in (-\pi/2, \pi/2)$), $\theta_{\text{in}} \in [0, \pi/2)$, $\theta_{\text{out}} \in (\theta_{\text{in}}, \pi/2)$, and $\log \dot{M}/M_{\odot} \text{ yr}^{-1} \in (-1, 3)$. In particular, we note that the range of mass outflow rate is broad enough to encompass pretty much all previously reported results in Muratov et al. [2015]; Fluetsch et al. [2019]; Roberts-Borsani and Saintonge [2019]; Roberts-Borsani et al. [2020]; Roberts-Borsani [2020]. For the likelihood, as we compare our model to the observations on a spectrum-by-spectrum basis, the total likelihood function is given by the product of single likelihood over all sky positions and velocity bins, so

$$\ln P(f_{\text{obs}}|\phi, \theta_{\text{in}}, \theta_{\text{out}}, \log \dot{M}) = -\frac{1}{2} \sum_i \sum_j \frac{(f_i(v_j; \phi, \theta_{\text{in}}, \theta_{\text{out}}, \log \dot{M}) - f_{i,\text{obs}}(v_j))^2}{\sigma_{ij}^2} \quad (2.8)$$

where f_i and $f_{i,\text{obs}}$ represent the predicted and observed spectra at the i th position (i.e., at the i th box shown in Figure 2.1), the spectra are measured at velocities v_j , and σ_{ij} is the observational uncertainty at position i and velocity bin j . The posterior PDF can then be calculated via Bayes' theorem

$$P(\phi, \theta_{\text{in}}, \theta_{\text{out}}, \log \dot{M}|f_{\text{obs}}) \propto P(f_{\text{obs}}|\phi, \theta_{\text{in}}, \theta_{\text{out}}, \log \dot{M}) P_{\text{prior}}(\phi, \theta_{\text{in}}, \theta_{\text{out}}, \log \dot{M}) \quad (2.9)$$

We calculate the posterior probability distribution function, from which we determine the best-fitting parameters with their uncertainties, using the affine-invariant Markov Chain Monte Carlo (MCMC) ensemble sampler EMCEE [Foreman-Mackey et al., 2013]. For each combination of driving mechanism, potential and expansion law, we use 40 MCMC walkers, each iterating over 500 steps to sample the posterior distribution of parameters. In general, the distribution of walkers needs ~ 50 iterations to stabilise, so we burn in the first 100 iterations and derive the posterior PDFs from the rest.

2.3.2 Which combination of driving mechanism, potential and expansion law?

Having optimised physical parameters for all combinations of the driving mechanism, potential, and expansion law, denoted as (dm, p, ex) , we are now in a position to distinguish which combination gives the best fit to the observed data. In order to decide this, for each combination (dm, p, ex) , we find the largest value of the likelihood function returned by any of the MCMC sample points, denoted as $\hat{\mathcal{L}}_{(dm,p,ex)}$, and compute the corresponding Akaike information criteria (AIC) (see [Sharma, 2017])

$$AIC_{(dm,p,ex)} = 2k - 2 \ln \hat{\mathcal{L}}_{(dm,p,ex)} \quad (2.10)$$

where $k = 4, 5$ and 5 are the number of parameters for ideal, radiation and hot gas driven winds, respectively: 3 parameters to describe the cone sheath geometry, 1 parameter to describe the mass-outflow rate, and 1 extra parameter to describe the optical depth or hot gas velocity for the radiation-driven or hot gas cases, respectively. The corresponding Akaike weight for each combination then is

$$w(dm, p, ex) = \frac{e^{-\Delta_{(dm,p,ex)}/2}}{\sum_{(dm,p,ex)} e^{-\Delta_{(dm,p,ex)}/2}} \quad (2.11)$$

$$\Delta_{(dm,p,ex)} = AIC_{(dm,p,ex)} - \min \left(AIC_{(dm,p,ex)} \right)$$

which gives the relative probability for each combination of driving mechanism, potential, and expansion law.

Results

In this section, we fit our model to the observations of multi-phase outflows in M82 in order to constrain its kinematics, geometry, and mass flux. We make use of recent resolved wide-field maps of the H I 21cm line [Martini et al., 2018] and CO J=2→1 transition line [Leroy et al., 2015], which provide us with unprecedented spatial and spectroscopic information about the wind. Our strategy is as follows: for each phase of outflow in M82, we optimise parameters describing the geometry and mass outflow rate, for all the combinations of driving mechanism, potential, and expansion law. We then investigate which combination and set of parameters gives the best recovery of the spectroscopic map, both based on the statistical tools and direct visual comparison. We then test the ability of the model to reproduce the data more broadly, by investigating which features in the data the model can or cannot produce. We conclude this section by digging into the reasons why certain parameters, driving mechanisms, potentials, and expansion laws are favored by the observations, and discuss at what level of confidence we could believe in our results.

We introduce the basic set up of the model galaxy, upon which all our analyses are based, in Section 3.1. Section 3.2 shows our fits for H I 21 cm line and Section 3.3 shows those for CO 2 → 1 transition line.

3.1 Model galaxy

We set the basic physical parameters of our M82 model to the same values adopted in Krumholz et al. [2017b], except for the parameters we would like to fit. Specifically, we adopt $r_0 = 250\text{pc}$ to be the radius of star-bursting center [Kennicutt, 1998] and take the escape speed to be $v_0 = 170\text{ km s}^{-1}$ [Greco et al., 2012], corresponding to a dynamical mass of $M_0 = 8.2 \times 10^8 M_\odot$. M82’s star formation rate is $\dot{M}_* = 4.1 M_\odot \text{yr}^{-1}$ assuming Chabrier [2005] IMF [Kennicutt, 1998]. The gas velocity dispersion in the disc is measured to be $\sim 40\text{ km/s}$ [Leroy et al., 2015] and the gas temperatures are $T = 5000\text{ K}$ for warm neutral phase, corresponding to a Mach number of $\mathcal{M} = 7.4$. For cold molecular phase we set the gas temperature to be $T = 50\text{ K}$ [Wild et al., 1992] corresponding to a Mach number of $\mathcal{M} = 100$.

| HI 21cm [Martini et al., 2018] | | | | | | | | | |
|--------------------------------|------------|--------------|-----|----------------------------|---------------------------|--------------------------|------------------------|---------------------------|--------------------------|
| dm | Models | exp law | w | ϕ | θ_{in} | Best fit parameters | | | |
| | pot | | | | | θ_{out} | $\log \dot{M}$ | τ_0 | u_h |
| North | | | | | | | | | |
| ideal | point | area | 0 | $1.00^{+1.87}_{-2.18}$ | $32.33^{+1.78}_{-1.53}$ | $89.02^{+0.68}_{-2.71}$ | $0.61^{+0.02}_{-0.02}$ | - | - |
| | | intermediate | 0 | $-34.09^{+75.05}_{-1.93}$ | $38.13^{+2.63}_{-2.07}$ | $73.00^{+3.03}_{-6.23}$ | $1.46^{+0.04}_{-0.07}$ | - | - |
| | | solid angle | 0 | $-42.46^{+92.74}_{-6.35}$ | $46.27^{+2.94}_{-13.26}$ | $70.43^{+4.26}_{-5.29}$ | $1.81^{+0.03}_{-0.17}$ | - | - |
| | isothermal | area | 0 | $-0.40^{+2.31}_{-2.19}$ | $13.83^{+2.40}_{-2.62}$ | $87.73^{+1.52}_{-4.83}$ | $1.62^{+0.02}_{-0.05}$ | - | - |
| | | intermediate | 0 | $1.06^{+2.00}_{-2.31}$ | $30.09^{+1.15}_{-0.95}$ | $85.69^{+3.09}_{-5.18}$ | $0.87^{+0.03}_{-0.04}$ | - | - |
| | | solid angle | 0 | $-35.94^{+87.57}_{-8.21}$ | $42.71^{+2.91}_{-11.58}$ | $70.02^{+4.09}_{-5.09}$ | $1.73^{+0.04}_{-0.14}$ | - | - |
| radiation | point | area | 1 | $1.73^{+3.58}_{-3.79}$ | $57.29^{+5.50}_{-5.87}$ | $78.98^{+5.53}_{-5.52}$ | $0.74^{+0.04}_{-0.05}$ | $65.55^{+18.80}_{-39.21}$ | - |
| | | intermediate | 0 | $-10.47^{+52.72}_{-25.32}$ | $34.04^{+6.63}_{-10.19}$ | $69.88^{+5.14}_{-9.19}$ | $1.44^{+0.04}_{-0.32}$ | $76.12^{+15.39}_{-20.02}$ | - |
| | | solid angle | 0 | $-37.78^{+39.39}_{-12.27}$ | $51.03^{+10.65}_{-29.47}$ | $71.08^{+8.35}_{-14.08}$ | $1.59^{+0.12}_{-0.13}$ | $77.49^{+8.81}_{-16.01}$ | - |
| | isothermal | area | 0 | $-5.24^{+3.12}_{-1.86}$ | $33.05^{+23.43}_{-1.85}$ | $83.06^{+5.85}_{-10.55}$ | $1.73^{+0.18}_{-0.07}$ | $71.58^{+19.43}_{-25.99}$ | - |
| | | intermediate | 0 | $0.92^{+2.05}_{-2.35}$ | $30.14^{+1.33}_{-0.93}$ | $85.72^{+3.08}_{-5.80}$ | $0.88^{+0.04}_{-0.05}$ | $78.62^{+13.51}_{-16.79}$ | - |
| | | solid angle | 0 | $-16.41^{+61.63}_{-27.23}$ | $22.39^{+18.59}_{-11.30}$ | $59.45^{+14.22}_{-6.60}$ | $0.96^{+0.26}_{-0.15}$ | $22.33^{+40.97}_{-4.61}$ | - |
| hot gas | point | area | 0 | $-2.53^{+11.25}_{-26.96}$ | $10.65^{+17.03}_{-6.98}$ | $87.90^{+1.49}_{-3.18}$ | $0.57^{+0.09}_{-0.04}$ | - | $14.83^{+13.75}_{-3.85}$ |
| | | intermediate | 0 | $-32.61^{+85.57}_{-6.37}$ | $37.73^{+4.62}_{-9.46}$ | $66.98^{+6.29}_{-13.86}$ | $1.43^{+0.15}_{-0.39}$ | - | $7.99^{+2.64}_{-2.42}$ |
| | | solid angle | 0 | $-23.88^{+81.35}_{-25.93}$ | $47.83^{+5.67}_{-19.81}$ | $66.36^{+7.80}_{-4.98}$ | $1.82^{+0.11}_{-0.30}$ | - | $13.43^{+6.17}_{-4.48}$ |
| | isothermal | area | 0 | $1.92^{+4.65}_{-2.14}$ | $31.89^{+2.66}_{-1.42}$ | $70.10^{+16.60}_{-7.79}$ | $1.64^{+0.11}_{-0.08}$ | - | $8.51^{+3.59}_{-1.37}$ |
| | | intermediate | 0 | $-19.68^{+18.43}_{-21.57}$ | $9.67^{+7.87}_{-3.69}$ | $88.20^{+1.35}_{-2.77}$ | $0.88^{+0.03}_{-0.06}$ | - | $23.95^{+4.27}_{-6.23}$ |
| | | solid angle | 0 | $36.88^{+93.95}_{-12.75}$ | $44.33^{+5.73}_{-13.94}$ | $64.06^{+7.82}_{-6.51}$ | $1.74^{+0.17}_{-0.26}$ | - | $9.81^{+2.78}_{-3.29}$ |

Table 3.1: Best-fitting parameters and Akaike weights obtained for all combinations of driving mechanism (Column 1), potential (Column 2) and expansion law (Column 3) for the warm neutral phase outflow. We highlight the case that gives the highest Akaike weight. Values are specified in the form $p(50)^{p(84)-p(50)}_{p(16)-p(50)}$, where $p(q)$ is the q th percentile of the marginalised posterior PDF for that quantity. The first three Column 1: driving mechanism; Column 2: gravitational potential; Column 3: cloud expansion law;

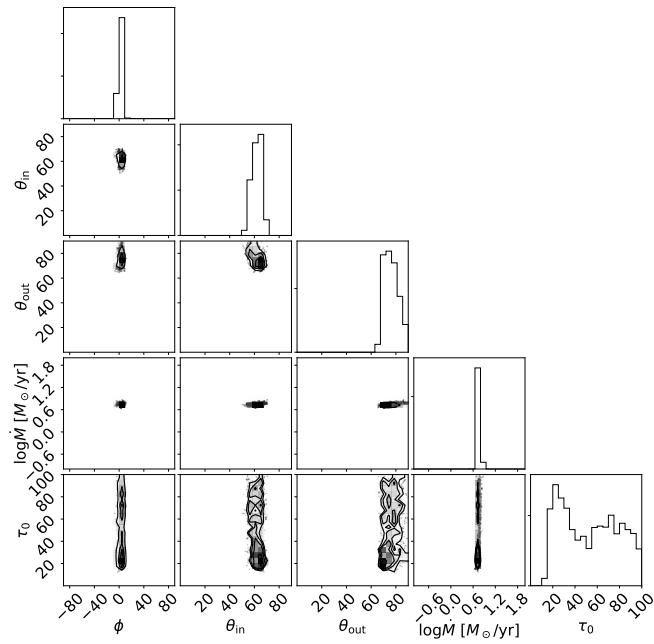


Figure 3.1: Corner plot showing the 1D and 2D histograms of the posterior PDFs of the parameters ϕ , θ_{in} , θ_{out} , $\log \dot{M}$ and τ_0 of the warm neutral phase outflow, as determined by MCMC optimisation. Histograms show 1D marginal PDFs for each parameter; 2D maps show 2D probability densities. The model fit shown is for a radiatively-driven wind in a point gravitational potential, for clouds that maintain constant area as they flow outward; this combination of driving, potential, and cloud expansion yields the highest Akaike weight as compared to other combinations.

3.2 Warm neutral phase

We first present our fits for warm neutral phase outflow as traced by the H I 21 cm observations. We show the set of best-fit parameters with their uncertainties and the Akaike weights for all combinations of the driving mechanism, expansion law and potential in Table 3.1. From the Akaike weight in the table, we find that a radiatively driven wind in a point gravitational potential, with clouds that maintain constant area, provides the best fit to the data. We explore the implications of our best-fitting parameters for this case in Section 3.2.1, validate our model in Section 3.2.2 and compare our fits with different combinations of driving mechanism, potential and expansion law in Section 3.2.3

3.2.1 Best-fitting physical parameters

For radiatively driven, point potential and constant area expansion, the combination of driving mechanism, potential, and expansion law for which we find the highest Akaike weight, Figure 3.1 shows the 1D and 2D histograms of the marginalised posterior PDFs of the five parameters ϕ , θ_{in} , θ_{out} , $\log \dot{M}$ and τ_0 as determined from our MCMC samples. We see that these parameters are well constrained and largely non-degenerate, with all of them converged into a tiny island of parameter space with the exception of τ_0 , which is simply constrained to be $\gtrsim 20$. Our best-fitting parameters values are largely consistent with and extend the results of previous observational studies. The near-zero orientation angle ϕ indicates the edge-on nature of the M82 and the large opening angle θ_{in} and θ_{out} implies the cone sheath geometry of galactic outflow, which has not been proposed before. The mass outflow rate at the nuclear region is about $5.50 M_{\odot}/\text{yr}$, corresponding to the mass-loading factor of $\eta_{\text{wn}} = \dot{M}/\dot{M}_{*} \approx 1.34$, which is within the range of values derived in previous literature [Strickland and Heckman, 2009].

3.2.2 Model validation

Before accepting the best-fitting parameters we have obtained as definitive, it is important to establish that the our parametric model gives a reasonable description of that data. To this end, we compare spectra predicted by our parametric model to the observed ones in Figure 3.2. In this figure, the grey band shows the observed spectrum (with 1σ errors) at each of our sample positions, while the orange lines show predicted spectra computed using parameters from 5 randomly-selected walkers at the final iteration of the MCMC. We see that the theoretical spectra give a fairly good fit to the observations at all positions, both in strength and shape.

In order to explore how well the model can discriminate between different parameter values, Figure 3.3 gives us a view on how the quality of the fits varies with the change of each parameter, which we will discuss in turn. The purpose of this exercise is not simply to justify the tight parameter constraints shown in Figure 3.1, but to provide some insight into what features of the spectra the model is using to constrain particular model parameters.

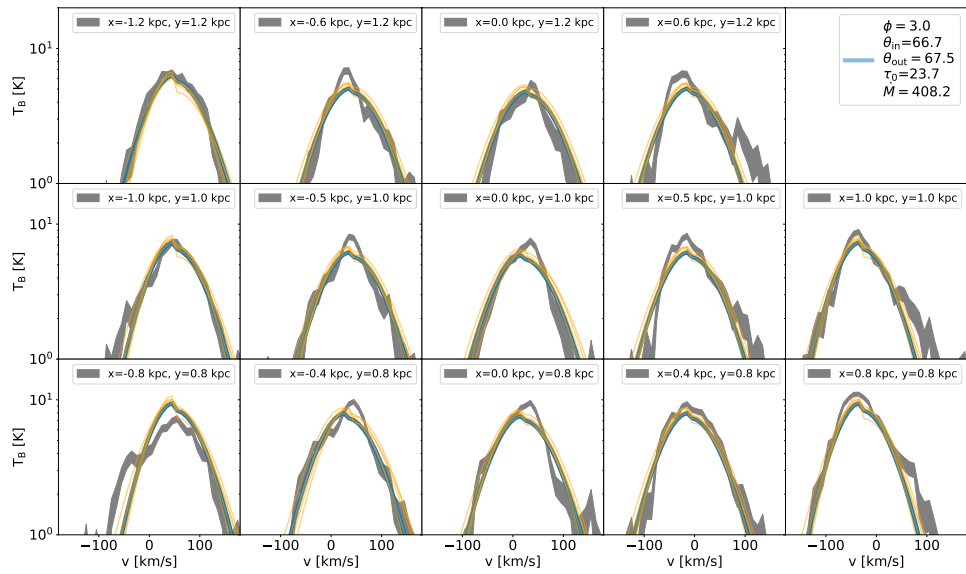


Figure 3.2: Predicted versus observed HI 21 cm spectra; each panel shows the spectrum at one of our sample positions, expressed as brightness temperature T_B as a function of velocity v , with $v = 0$ corresponding to the systemic velocity of M82. The lines shown are the predicted spectra adopting the value of parameters that gives the maximum value of likelihood function in MCMC (blue line), and using the parameters from 5 random walkers at the last iteration of MCMC sampling (orange lines). For comparison, we also show the observed spectrum with its 1σ error (grey region).

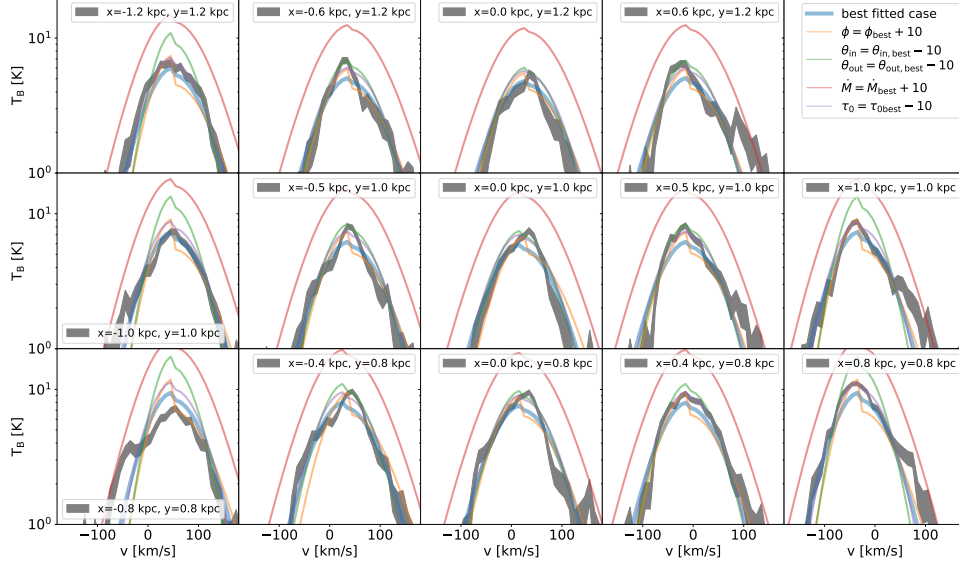


Figure 3.3: Same as Figure 3.2, but now showing how the predicted spectra vary in response to changes in the fit parameters. The best-fit case is shown by the blue line and the observed spectrum with 1σ errors is shown by the grey region, as in Figure 3.2, while spectra produced by varying ϕ , θ_{in} with θ_{out} , \dot{M} and τ_0 are shown in orange, green, red and purple, respectively.

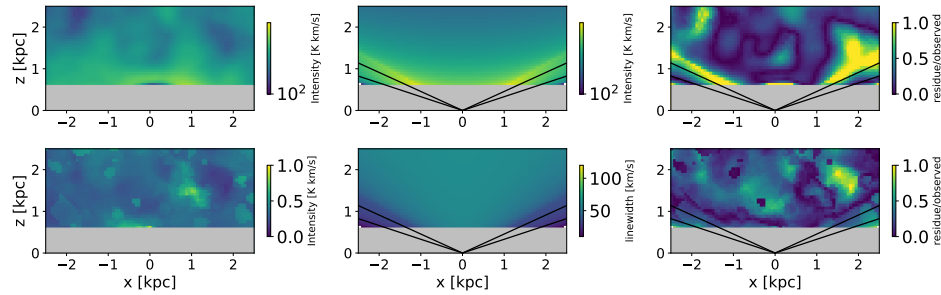


Figure 3.4: Velocity-integrated intensity (top row) and brightness temperature weighted second moment map (bottom row) for the observations (left), theoretical predictions using our best-fitting model (middle) and the residual between the two (right) for HI 21 cm line. The black lines show our best-fitting angles θ_{in} and θ_{out} for the inner and outer angles of the outflow cone. The grey central region is a mask to block out 0.6 kpc around the galactic disc.

We first increase the orientation angle ϕ by 10 degrees, thereby inclining the outflow axis more relative to the plane of the sky. We see that the increased value of ϕ gives rise to an asymmetry in the spectra. The reason for this is simple: positive velocities correspond to the far side of outflow while negative velocities correspond to the near side. A small value of ϕ means we are observing both near and far side of wind at similar distances from the nuclear region, so only optical depth effects, which are negligible in the case of H I, could induce asymmetry between the negative and positive velocity sides of the spectra. However, for non-zero ϕ , our line of sight passes through the the near and far sides of the outflow at two different distances from the nucleus. The near and far sides therefore have different emissivities, leading to a sharp change in the spectrum near zero velocity. Such a sharp feature is not observed, which is why our model prefers an orientation angle ϕ close to zero.

We next jointly investigate the changes caused by the variations in θ_{in} , θ_{out} and τ_0 . To this end, we plot example predictions for which the opening angles θ_{in} and θ_{out} have been reduced by 20° and 10° compared to the best-fitting case, respectively. We see that the effect of this change is that line the profile becomes narrower for lines of sight close to the central axis of the wind (e.g., $(x, y) = (0, 1)$ kpc), but and both becomes narrow and much more intense near $v = 0$ for lines of sight farther from the central axis (e.g., $(-1, 1)$ kpc). The physical origin of this behaviour is that, as we narrow the outflow cone, we both reduce the amount of material travelling close to along the line of sight (thus depressing the high-velocity wings of the line) and create lines of sight that remain inside the outflow cone over much longer distances, increasing the intensity. Thus both the shape of the line winds and the amount of variation in intensity from one line of sight to another serve to constrain the opening angle. Decreasing τ_0 from ≈ 23 to ≈ 13 has a somewhat similar effect as the lower optical depth makes it harder to accelerate material to high speed, and therefore suppresses the line wings. Surprisingly, it seems like there is little degeneracy between the opening angle and optical depth even they play a similar role in setting the linewidth. The reason for this is that τ_0 will only affect the tail of spectra that is nearly close to the asymptotic velocity, while the opening angle changes the overall geometric shape of the outflow and will affect the spectra over a much wider velocity range. Hence in Table 3.1 we see that even in fits with radiation and hot gas driven prescription, there is a similar uncertainty in these two opening angles compared to ideal cases.

Finally, we see that the mass outflow rate acts as a normalisation of the spectra, which affects the overall intensity rather than the shape of the profile. With increased \dot{M} , the generated spectra overestimate the observed ones at nearly all velocity bins and all positions. In sum, we see that our model is able to capture the rich information hidden in the spectra, exploiting the fact that each parameter is responsible for different features, with ϕ setting the asymmetry of the profile, θ_{in} , θ_{out} and τ_0 setting the line-width and \dot{M} controlling the overall scaling.

Having shown that our model can provide a reasonable fit to all these representative spectra, our final validation test is to investigate whether our fits give a good match to the entire 2D map, or, in other words, whether our model can reproduce

the data that is not included in the fits. To investigate this, we check the degree of consistency between predicted and observed velocity-integrated quantities across the whole region. Specifically, we compare the integrated intensity and intensity-weighted second moment map of model and observation in Figure 3.4. In this figure, we mask the central region from 0 to 0.6 kpc in the vertical axis to avoid contamination from the disc region. Outside the masked region, we see that the predicted and observed maps show similar morphology and absolute value, particularly near the minor axis, illustrating that our model reproduces the structure for the bulk of the outflow. However, there are some tensions near the inner boundary of the outflow cone, as illustrated by the black lines in the figure. In particular, we see that our model predicts significantly more limb-brightening than is observed in the integrated-intensity map, and a sharper decrease in second moment as one moves away from the central axis. This may be due to our oversimplification of the true geometry, as we assume there is a hard cutoff of wind material at the inner and outer boundary. At a given height, this feature of our model implies increasing LOS distance and decreasing velocity range as the impact parameter (x) approaches the inner cone, which overestimates the velocity-integrated intensity and underestimates the second moment. This artificial boundary effect is not present in real galaxies, as the geometry is more likely to resemble a biconical frustum (for which the “base” in the plane of the galaxy is a disc of finite area, rather than a point), and the boundary of the volume occupied by H I is much less sharp than in our idealised model.

3.2.3 Driving mechanism, potential and expansion law

Having illustrated why certain parameters are favored for the combination of radiative driving, point gravitational potential, and constant area expansion law that yields the highest Akaike weight, we now return to explore why our modeling favours this combination of driving mechanism, potential, and expansion law over the alternatives we have tried.

We start with the two choices that will cause the largest variation to the physical nature of the outflow and the shape of the spectra, which are the potential and expansion law. As a reminder, the choice of potential describes the shape of the gravitational potential, and thus the rate of gravitational deceleration, as the wind moves out – a point potential corresponds to a gravitational force that diminishes as $1/r^2$ (as would be expected if the mass decelerating the outflow is mostly concentrated in the galaxy itself), while an isothermal potential corresponds to $1/r$ (as would be expected if the dark matter halo dominates the deceleration). Similarly, the expansion law dictates how clouds’ cross-sectional areas, and thus the amount of momentum per unit time they intercept from the wind driving mechanism, change as they flow outward; constant area and constant solid angle are the two extremes, and intermediate representing the geometric mean of the two. Together these choices dictate much of the physical nature of the wind, and this in turn manifests in the MCMC fitting. For example, consulting Table 3.1, we see that all wind models (models where the outflow escapes to infinity, which happens for either constant solid angle clouds

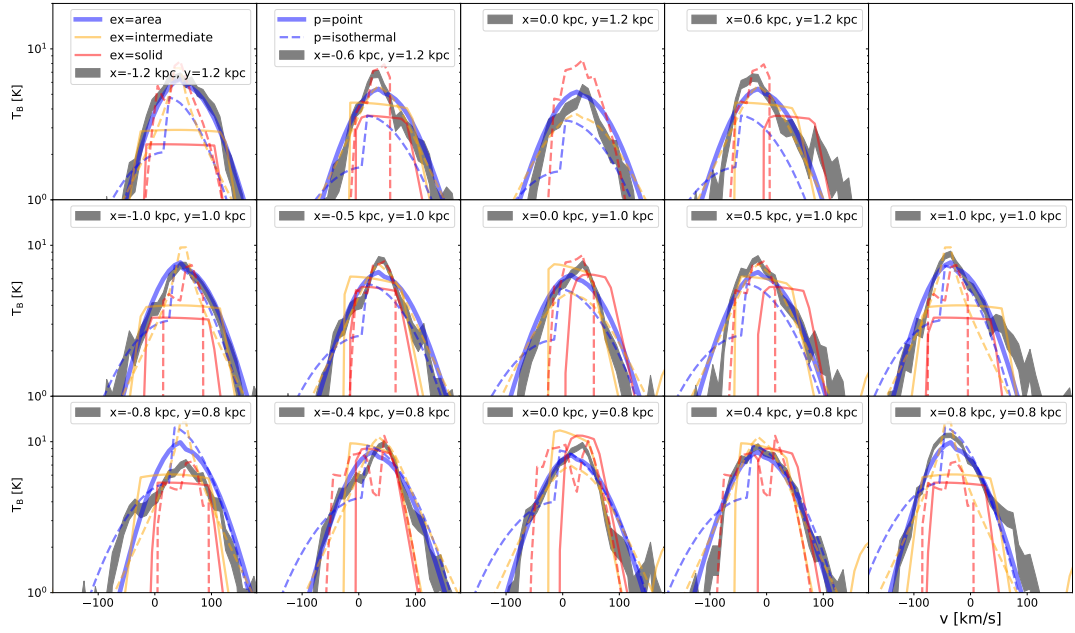


Figure 3.5: Same as Figure 3.2, but now showing how the predicted spectra vary in response to the choices of potential and expansion law, for radiatively driven winds. We show the best-fitting spectra for each individual combination of potential and expansion law. The spectrum produced with the combination that yields the highest Akaike weight is shown by the thickest line and the observed spectrum with 1σ errors is shown by the grey region, as in Figure 3.2. Spectra adopting point and isothermal gravitational potential are shown in solid and dashed lines, while those adopting constant area, intermediate, and constant solid angle expansion laws are shown in blue, yellow and red line, respectively.

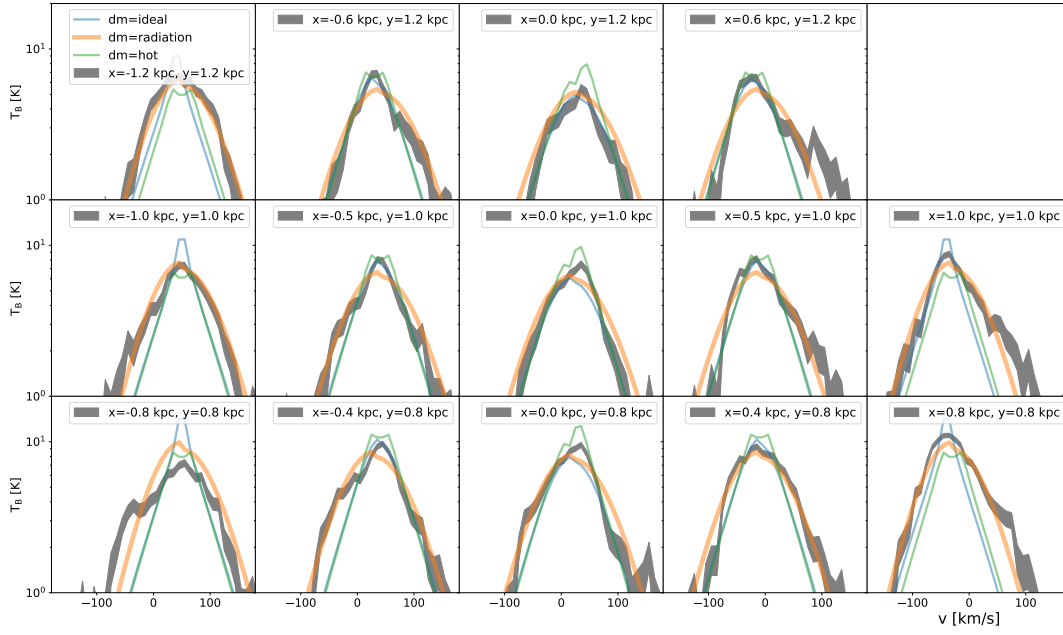


Figure 3.6: Same as Figure 3.2, but now showing how the predicted spectra vary in response to the choices of driving mechanism, for point gravitational potential and constant area expansion. We show the best-fitted spectra for each individual driving mechanism. The spectra produced with the combination that yields the highest Akaike weight is shown by the thickest line and the observed spectrum with 1σ errors is shown by the grey region, as in Figure 3.2, while spectra adopting ideally, radiatively and hot gas driven wind are shown in blue, orange and green, respectively.

or for clouds with intermediate expansion in a point potential) yield unrealistically large orientation angles $\phi \sim \pm 40^\circ$ with a huge uncertainty, while fountain models where the wind does not escape (all others) yield $\phi \approx 0$, consistent with the edge-on nature of M82. The reason for this is simple: we observe emission near zero velocity, which implies either that gas launched in the wind eventually decelerates to zero velocity, as happens in a fountain, or that we are seeing gas whose velocity is solely along the plane of sky and hence has zero projection on the LOS. As the gas is constantly being accelerated in the wind scenario, leaving no gas whose radial velocity is zero, the MCMC attempts to compensate for this by fitting a large orientation angle, so that one side of the wind is flowing nearly on the plane of sky. However, this compensation worsens the fit to the remainder of the spectrum, yielding a lower Akaike weight overall.

We illustrate this effect in Figure 3.5, which shows us how the quality of fits varies with the different choices of potential and expansion law, for radiatively driven winds. For each combination of driving mechanism and expansion law, we plot the model with the highest likelihood recovered by the MCMC. We see that although all models produce near zero-velocity emission, the wind models clearly show a deficit of emission at the centre, and a line shape function completely different to that of the observed spectra. In contrast, fountain models provide a much better comparison to the observations, both at line centre and line wings, and yield Akaike weights that are orders-of-magnitude higher than those of the wind models. Our method is able to distinguish between winds and fountains with great confidence.

The difference between various types of fountain models, for example constant area expansion with a point versus an isothermal potential, is somewhat more subtle, but still noticeable, and allows the MCMC fit to distinguish clearly between models. For example, an isothermal potential gives rise to a much larger asymmetry between positive and negative velocities than the point potential; the physical reason is that the wind cone is slightly tilted relative to the line of sight, so along a given line of sight, the material at positive velocity is at a slightly different distance from the launching point than the material at negative velocity, resulting in a velocity difference. The size of the difference, in turn, depends on how quickly the wind decelerates, and is larger for the stronger deceleration provided by an isothermal potential.

We next deal with the choices that will calibrate the line wings of the spectra, which is the driving mechanism. We illustrate how the quality of fits varies with the different choices of driving mechanism, for point gravitational potential and constant area expansion, in Figure 3.6. For each driving mechanism, we plot the model with the highest likelihood recovered by the MCMC. We clearly see radiatively-driven wind reproduced the line wings at nearly all positions, whereas other two models both show a deficit at the line wings and overweigh the peak at the centre. Our method is able to distinguish between driving mechanism with great confidence.

| CO J=2→1 [Leroy et al., 2015] | | | | | | | | | |
|-------------------------------|------------|--------------|------|----------------------------|---------------------------|---------------------------|-------------------------|---------------------------|--------------------------|
| Dm | Models | Exp law | w | ϕ | θ_{in} | θ_{out} | log \dot{M} | τ_0 | u_h |
| North | | | | | | | | | |
| ideal | point | area | 0 | $1.86^{+0.22}_{-3.20}$ | $34.97^{+11.17}_{-0.23}$ | $69.70^{+4.96}_{-0.46}$ | $-0.06^{+1.83}_{-0.01}$ | - | - |
| | | intermediate | 0 | $-2.02^{+49.01}_{-25.26}$ | $13.75^{+15.55}_{-12.32}$ | $60.27^{+15.05}_{-7.07}$ | $0.36^{+0.15}_{-0.06}$ | - | - |
| | | solid angle | 0 | $-47.60^{+101.85}_{-8.04}$ | $43.63^{+2.27}_{-6.17}$ | $74.97^{+1.52}_{-4.84}$ | $0.80^{+0.02}_{-0.03}$ | - | - |
| | isothermal | area | 0 | $0.11^{+1.34}_{-2.87}$ | $28.80^{+0.85}_{-0.74}$ | $77.53^{+5.77}_{-7.36}$ | $0.53^{+0.03}_{-0.03}$ | - | - |
| | | intermediate | 0 | $-1.25^{+2.53}_{-4.55}$ | $7.63^{+15.22}_{-2.76}$ | $87.90^{+1.51}_{-12.98}$ | $-0.12^{+0.04}_{-0.02}$ | - | - |
| | | solid angle | 0 | $-49.60^{+100.45}_{-2.51}$ | $40.90^{+2.01}_{-4.99}$ | $75.54^{+1.78}_{-2.97}$ | $0.75^{+0.02}_{-0.03}$ | - | - |
| radiation | point | area | 0.03 | $-1.04^{+2.62}_{-3.43}$ | $31.30^{+19.98}_{-2.16}$ | $76.37^{+7.18}_{-7.71}$ | $-0.09^{+0.22}_{-0.03}$ | $-88.04^{+4.53}_{-16.63}$ | - |
| | | intermediate | 0 | $0.00^{+22.14}_{-4.22}$ | $2.50^{+21.70}_{-1.95}$ | $60.21^{+17.44}_{-2.69}$ | $0.19^{+0.25}_{-0.04}$ | $88.75^{+8.89}_{-26.81}$ | - |
| | | solid angle | 0 | $1.00^{+43.62}_{-37.14}$ | $23.91^{+9.67}_{-23.39}$ | $67.26^{+11.11}_{-15.51}$ | $0.30^{+0.29}_{-0.37}$ | $87.88^{+10.63}_{-16.63}$ | - |
| | isothermal | area | 0.57 | $-0.52^{+1.72}_{-1.47}$ | $29.19^{+1.11}_{-15.84}$ | $80.07^{+5.29}_{-5.13}$ | $0.53^{+0.04}_{-0.05}$ | $75.18^{+12.83}_{-15.05}$ | - |
| | | intermediate | 0 | $0.94^{+2.46}_{-2.73}$ | $29.58^{+20.52}_{-12.00}$ | $84.59^{+3.73}_{-8.93}$ | $0.07^{+0.39}_{-0.05}$ | $96.40^{+2.93}_{-33.80}$ | - |
| | | solid angle | 0 | $1.86^{+55.07}_{-35.23}$ | $27.33^{+5.82}_{-12.07}$ | $80.78^{+2.73}_{-3.73}$ | $0.14^{+0.05}_{-0.04}$ | $97.23^{+2.48}_{-10.59}$ | - |
| hot gas | point | area | 0.22 | $1.05^{+9.13}_{-4.87}$ | $5.20^{+37.32}_{-3.52}$ | $85.31^{+3.29}_{-18.59}$ | $-0.10^{+0.36}_{-0.03}$ | - | $13.99^{+11.49}_{-5.30}$ |
| | | intermediate | 0 | $-26.53^{+59.61}_{-4.79}$ | $27.97^{+7.63}_{-7.73}$ | $65.05^{+4.53}_{-5.38}$ | $0.60^{+0.10}_{-0.15}$ | - | $10.80^{+2.68}_{-3.00}$ |
| | | solid angle | 0 | $-15.21^{+71.64}_{-38.09}$ | $45.63^{+8.45}_{-14.92}$ | $69.19^{+6.25}_{-12.70}$ | $0.79^{+0.09}_{-0.17}$ | - | $9.02^{+1.75}_{-1.41}$ |
| | isothermal | area | 0 | $0.15^{+1.14}_{-2.38}$ | $29.39^{+0.85}_{-0.89}$ | $79.44^{+6.82}_{-7.74}$ | $0.57^{+0.06}_{-0.03}$ | - | $10.57^{+3.01}_{-4.01}$ |
| | | intermediate | 0.17 | $-13.11^{+15.53}_{-15.49}$ | $2.22^{+11.33}_{-1.67}$ | $85.99^{+2.69}_{-6.11}$ | $-0.10^{+0.03}_{-0.06}$ | - | $26.41^{+2.78}_{-12.46}$ |
| | | solid angle | 0 | $-39.61^{+92.10}_{-9.53}$ | $46.40^{+6.07}_{-13.70}$ | $68.07^{+6.28}_{-5.85}$ | $0.73^{+0.09}_{-0.16}$ | - | $11.13^{+0.74}_{-1.82}$ |

Table 3.2: Same as table 3.1, but show the results of fits for CO.

3.3 Cold molecular phase

We next present similar kind of analysis as in Section 3.2 for cold molecular phase outflow as traced by the CO J= 2 → 1 observations. We show the set of best-fit parameters with their uncertainties and the Akaike weights for all combinations of the driving mechanism, expansion law and potential in Table 3.2. From the Akaike weight in the table, we find that a radiatively driven wind in a isothermal gravitational potential, with clouds that maintain constant area, provides the best fit to the data. We explore the implications of our best-fitting parameters for this case in Section 3.3.1, validate our model in Section 3.3.2 and compare our fits with different combinations of of driving mechanism, potential and expansion law in Section 3.3.3.

3.3.1 Best-fitting physical parameters

For radiatively driven, isothermal potential and constant area expansion, Figure 3.7 shows the 1D and 2D histograms of the marginalised posterior PDFs of the five parameters ϕ , θ_{in} , θ_{out} , log \dot{M} and τ_0 as determined from our MCMC samples. Again, we see that these parameters converged into a tiny island of parameter space with the exception of τ_0 . We again find a near-zero orientation angle ϕ and reasonable values of opening angle θ_{in} and θ_{out} , verifies the cone sheath geometry of cold molecular phase outflow [Walter et al., 2017]. The mass outflow rate at the nuclear region is about $3.4M_{\odot}/\text{yr}$, corresponding to the mass-loading factor of $\eta_{\text{cm}} = \dot{M}/\dot{M}_{*} \approx 0.83$.

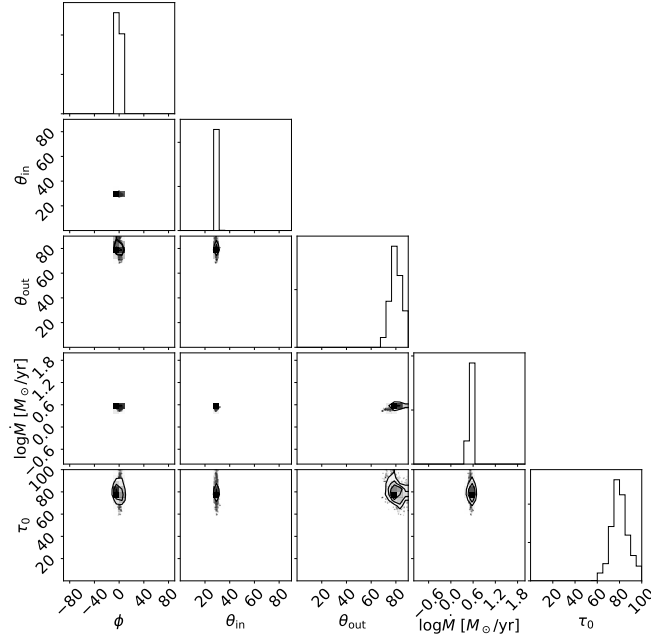


Figure 3.7: Same as figure 3.1, but show the results for CO.

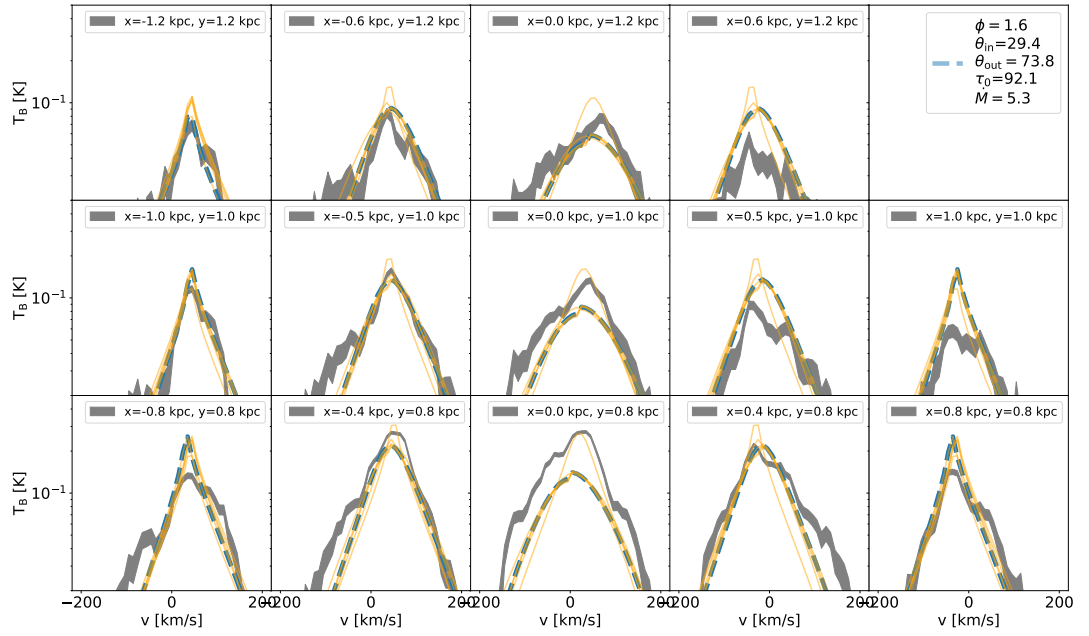


Figure 3.8: Same as figure 3.2, but show the results for CO.

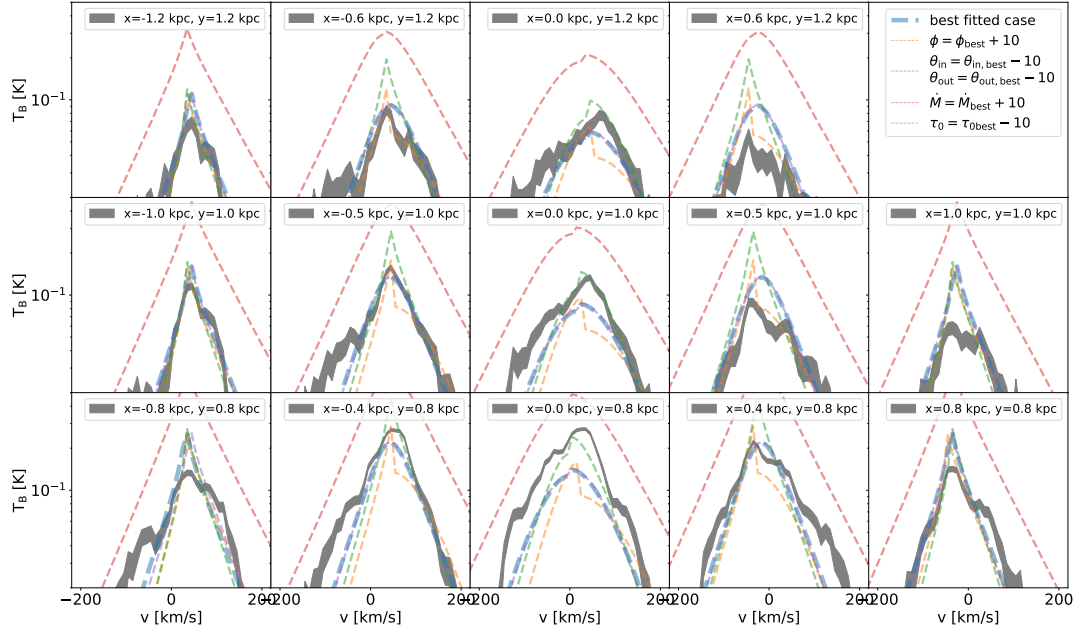


Figure 3.9: Same as figure 3.3, but show the results for CO.

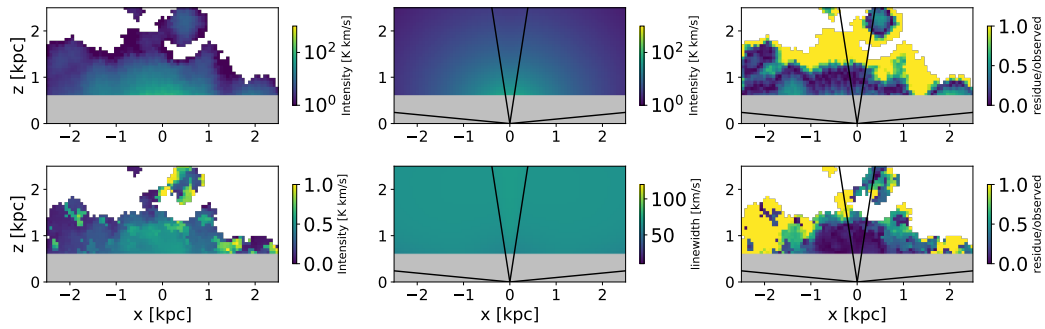


Figure 3.10: Same as figure 3.4, but show the results for CO.

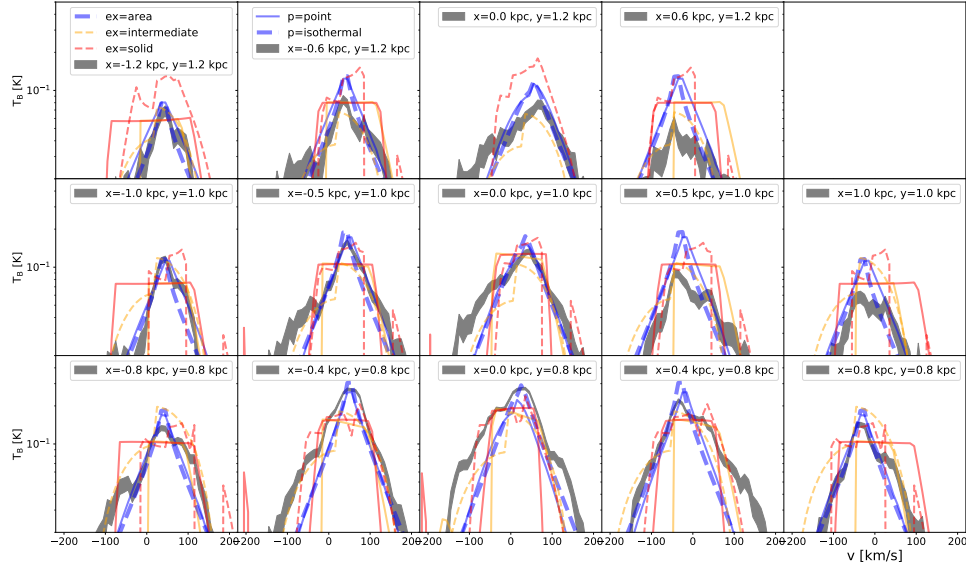


Figure 3.11: Same as figure 3.5, but show the results for CO.

3.3.2 Model validation

We present the same kind of analysis as in Section 3.2.2. We again compare predicted spectra, computed using parameters from 5 randomly-selected walkers at the final iteration of the MCMC, to the observed ones in Figure 3.8. We again see that the theoretical spectra give a fairly good fit to the observations at all positions. We next plot how the quality of the fits varies with the change of each parameter in Figure 3.9. We again see that our model is able to capture the rich information hidden in the spectra, with role of each parameter separated on creating these features.

We next test whether our fits give a fair match to the entire 2D map by comparing integrated intensity and intensity-weighted second moment map of both model and observation, in Figure 3.10. Outside the masked region, Our model reproduces the structure for the bulk of the outflow, particularly near the minor axis. However, we see that our model predict a shallower gradient in intensity than is observed in the integrated-intensity map, and a smoother change in second moment as one moves away from the central axis.

We see that the quality of fits for H I is significantly better than that for CO. This is due to the intrinsic complications of modeling CO lines, which requires us to make several approximations that may inevitably fail in some regime. First, the assumption of LTE is not valid for low density region of CO. Second, there is a complication in the Large Velocity Gradient approximation we used at evaluating optical depth effect, which may cause divergence at near zero velocity when thermal broadening becomes important.

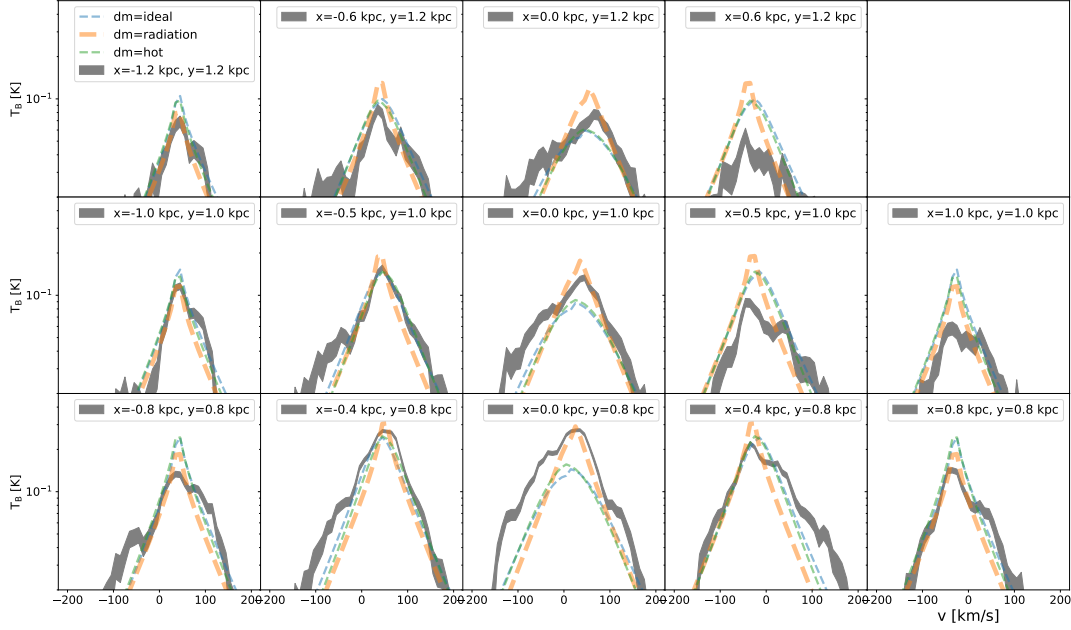


Figure 3.12: Same as figure 3.6, but show the results for CO.

3.3.3 Driving mechanism, potential and expansion law

We show how the quality of fits varies with the different choices of potential and expansion law, for radiatively driven winds in Figure 3.11. Our method again distinguishes between winds and fountains with great confidence. However, in this case, the difference between various types of fountain models, for example constant area expansion with a point versus an isothermal potential, is not clearly noticeable, and only allows for Akaike weight to distinguish between models. We next illustrate how the quality of fits varies with the different choices of driving mechanism, for isothermal gravitational potential and constant area expansion, in Figure 3.12. For each driving mechanism, we plot the model with the highest likelihood recovered by the MCMC. In this case, however, we do not get direct visual evidence that radiatively-driven wind reproduced the line wings while other two don't. Consulting Table 3.2, we also see that there is no order-of-magnitude difference in Akaike weight with the change of potential and driving mechanism. In sum, we conclude that CO $2 \rightarrow 1$ line can not distinguish different gravitational potential and driving mechanisms with a great confidence.

Discussion

Having presented our fits for the multi-phase outflow of M82, we are now in a position to interpret these results and come up with a physical picture of the cool wind in M82. We describe such a picture in Section 4.1, including clouds' evolution, comparison between multiple phases and the fate of outflowing cool gas in M82. We then discuss several caveats to our model and their possible effects on our results in Section 4.2.

4.1 A physical picture of cool winds in M82

We discuss the origin and the evolution of launched cool gas clouds in Section 4.1.1 and the fountain scenario in Section 4.1.2.

4.1.1 Origin and evolution of cool gas clouds

We first examine the primary source of the cool gas in the outflows. One scenario, proposed by Thompson et al. [2016], is that the cool gas in the galactic plane initially gets shock heated and mixed into the hot outflow, so that the gas leaving the galactic disc is almost entirely hot. The cool gas that we see above the plane then re-forms in-situ via radiative cooling of hot gas, and only appears far from wind launching region. In contrast, our model is based on an alternative scenario where a continuous population of cool clouds is accelerated from the central regions and survives their interactions with hot outflow. Our model therefore predicts the existence of a large amount of cool gas near the wind launching region, which is what we observed in M82. Our model therefore is more applicable to the central region of M82 than the model of [Thompson et al., 2016].

Our results further suggest that, when launched, these cold molecular and warm neutral clouds maintain approximately constant cross-sectional area as they propagate outwards, which implies that their morphologies are well-preserved through the entrainment processes. Previous theoretical studies have not reached consensus on whether, and under what circumstances, this is possible. Purely hydrodynamic simulations from Hopkins and Elvis [2010] show that Kelvin-Helmholtz (KH) instabilities stretches cold clouds and increases their cross-sectional area dramatically, while studies from [McCourt et al., 2015; Banda-Barragán et al., 2018; Zhang et al., 2017;

Grønnow et al., 2017] show that the magnetic pressure with $\beta \sim 1$ could suppress mixing [Gentry et al., 2019], confine the cloud expansion transverse to the direction of magnetic field, and allow the cloud to survive being entrained. Our results undoubtedly favor the latter scenario, and hence indicates that M82 is characterised by a strong magnetic field with field lines tracing the trajectory of launched clouds. This scenario is consistent with the recent measurements of magnetic field strength and morphology in M82 [Buckman et al., 2020; Yoast-Hull et al., 2013; Jones et al., 2019; Lopez-Rodriguez et al., 2021], which show that the magnetic field threads from starburst core all the way to intergalactic medium with a strength of $B \sim 300\mu\text{G}$ and $\beta \sim 0.7$.

4.1.2 Fountain scenario of M82

While our fits allow us to quantify with relatively small uncertainty how much gas the winds expel, we are left with another important question: what is the ultimate fate of the gas in the galactic winds in M82? Will it be driven out to the CGM or even further into IGM, or will it be captured by the gravitational potential and fall back as a fountain? Our finding that the molecular phase is best fit by the combination of isothermal potential and constant area expansion suggests that the outflow in M82 is a fountain [Krumholz et al., 2017b], which means all the molecular gas expelled by the central galaxy will ultimately fall back. To investigate how far the gas in M82 will go, we need to calculate how the mass-outflow rate decreases with the distance from the galaxy. Our calculations are as follows: we use the wind model parameters with the highest posterior probability from our MCMC samples to calculate the wind density and velocity structures. Now consider a parcel of gas that exits the wind launching region with dimensionless surface density $x = \ln(\Sigma/\bar{\Sigma})$, where $\bar{\Sigma}$ is the mean column density. Gas with higher surface density x will be driven to lower height, and when the gas surface density approaches $x_{\text{crit}} = \ln \Gamma$, the Eddington ratio, it will not be driven out at all. We can therefore calculate the height r_{turn} at which the gas with initial column density x will turn around. Conversely, this means that all gas with surface density below x will reach radius r_{turn} , while all the denser gas falls back. Therefore we find that at radius r , there is a cutoff column density $x_c(r)$ above which the gas will not be driven to that radius. Under the assumption of the steady-state outflow in our model, the mass outflow rate at a given radius is proportional to the fraction of mass that can reach that radius, so we can calculate the mass-outflow rate at radius r , $\dot{M}(r)$, via

$$\dot{M}(r) = f_A \dot{M} \frac{\int_{-\infty}^{x_c(r)} p_M(x) dx}{\int_{-\infty}^{x_{\text{crit}}} p_M(x) dx} \quad (4.1)$$

where $p_M(x)$ denotes the mass-weighted column density distribution at the wind launching region. We plot the mass-outflow rate versus the radius in blue lines in Figure 4.1. We see that the mass-outflow rate decreases from $3M_{\odot}/\text{yr}$ at $r \sim 0.25$ kpc to $0.6M_{\odot}/\text{yr}$ at $r \sim 3$ kpc, i.e. 80% of the gas falls back to the host galaxy before

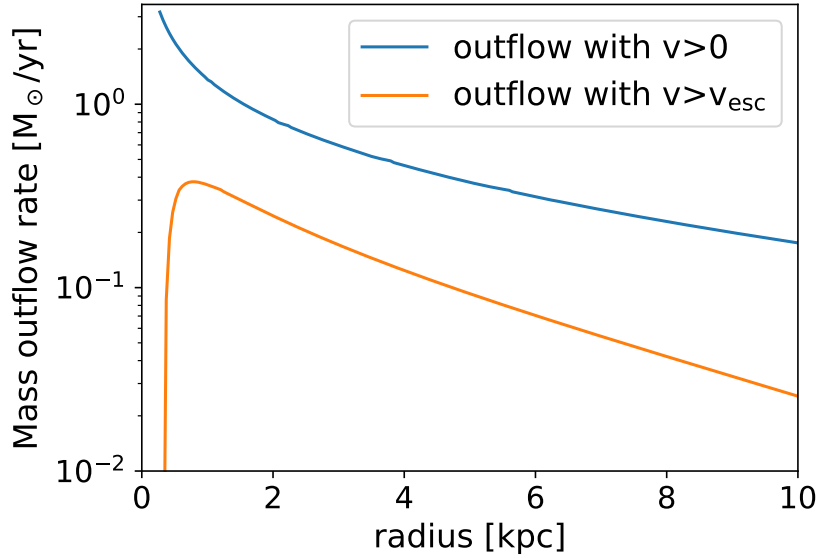


Figure 4.1: Molecular phase mass outflow rate as a function of radius. The blue line shows the total outflow rate whereas orange line shows the outflow rate only considering material moving faster than the escape velocity.

reaching 3 kpc height. If we define the effective scale height of the fountain as the height where the mass flux falls to $1/e$ of its value at launch, we find an effective scale height of ≈ 1.5 kpc.

A further implication of our model is that, although M82 is a fountain, we still observe emission at velocities above v_0 (the escape speed) in Figure 3.8. This finding challenges the commonly adopted strategy to distinguish the wind from fountain material by comparing the velocity with the escape speed. In the M82 molecular fountain, the gas may be driven to a speed higher than escape speed at some radius and nonetheless decelerate to zero speed and turn around at some larger radius. We investigate this issue by plotting the outflow rate of material with speed higher than the escape speed versus radius in orange lines in Figure 4.1. We also plot the fraction of material that moves faster than the escape speed as a function of radius r in Figure 4.2. We see that at small radius, almost none of the gas has been accelerated enough to exceed the escape speed. By radius of about 2 kpc, nearly 30% of the outflow material moves faster than the escape speed; however, our model suggests that all this gas will eventually fall back. In general, there is no correlation between the actual mass flux in the fountain, the fraction of material that moves at above the escape speed at any given radius, and the mass flux that will eventually escape the galaxy; it is not possible to distinguish fountains from winds based on velocity alone, without knowing the shape of the gravitational potential well outside the galaxy. This subtlety represents a challenge to future theoretical and observational study of outflows.

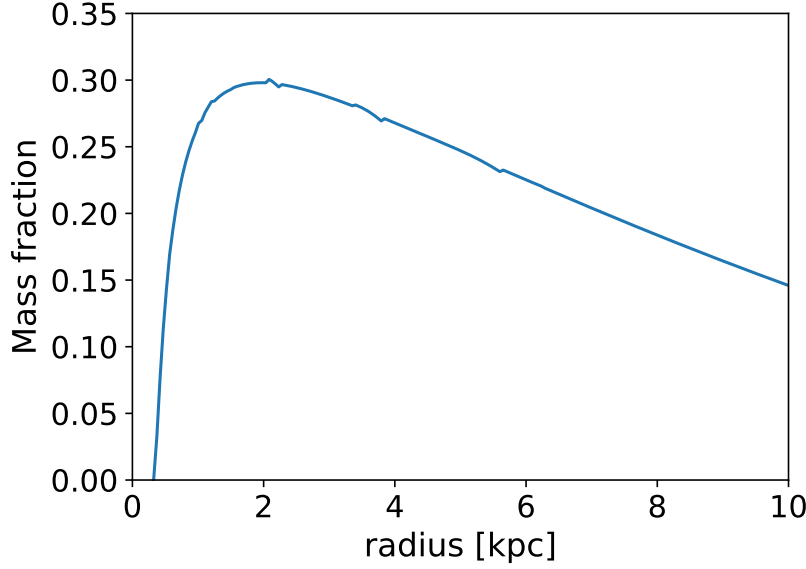


Figure 4.2: Fraction of the outflow material which moves faster than the escape speed as a function of radius. We see the acceleration processes increase the fraction of high velocity cloud at large radius of about 2 kpc.

4.2 Caveats

We end this chapter by noting several caveats for our results, as our analytical model inevitably ignore some key physics that will affect the underlying structure of our generated winds, both at galactic scale and cosmological scale.

The first limitation regards the simplified thermal and chemical structure adopted in our model, which assumes the each individual phase of cool wind is composed of a continuous population of clouds with a constant temperature and chemical composition that is independent of time and distance from the central galaxy. However, it is possible that galactic winds evolve in thermal or chemical properties as the they propagate outward. Depending on the nature of the change, this could either move gas into our out of the cool phases as the outflows propagate outward. The observed weak cooling in the wind of M82 found by [Hoopes et al., 2003] suggests a cooling of hot phases into the cool phase is unlikely to be a strong effect in this galaxy, but it is unclear if this result applies to outflows in general, or only to M82. Conversely, launched clouds may undergo chemical phase changes that dissociate molecular gas into neutral gas, which would cause the density of molecular gas to decrease much faster than that of neutral gas along the outflow. Similarly, some fraction of the neutral gas could be ionised, causing it to disappear in H I and appear in tracers of warm ionised gas such as H α . Determining how these thermal and chemical processes will affect the cool wind requires future observations of the chemical and thermal structure of the wind of M82 and a more accurate description of the thermal and chemical properties of the wind in our model.

The second limitation originates from our ignorance of the larger cosmological

environment around M82 that may induce complex structures in the real outflows that are not accounted for in our simple model. For example, the torque from M81 induces a tidal stream from M82, and this might alter the structure and distribution of matter in the outflow of M82. This is especially evident for warm neutral outflow traced by H I, as we can see in the form of the ‘northwest spur’ and ‘southeast spur’ induced by the drag exerted by ambient environment [Martini et al., 2018]. This ‘NW-SE’ asymmetry is in contrast with our model predictions, which is symmetric with the minor axis.

Conclusion

5.1 Summary

Despite recent high-resolution and sensitive observations of galactic winds that have given us rich sets of data, there is a lack of theoretical tools to extract information from them and interpret the results. In this thesis, we make a first step in this direction by applying a novel analytical model to constrain the kinematics of a multi-phase outflow with multi-wavelength observations in M82. We model the outflow as a continuous population of gas clouds being momentum-driven out of an isothermal turbulent medium in the galactic disc, and calculate the resulting winds' density and velocity structures. The kinematic structure is determined by model parameters describing geometry and mass outflow rate, and physics prescriptions for the driving mechanism, gravitational potential and cloud expansion law. We compare our model to H I and CO data on the wind of M82 on a spectrum-by-spectrum basis, well to the recent spatially resolved observations of galactic winds. We then constrain the physical parameters with a Bayesian approach and distinguish the best combination of driving mechanism, potential and expansion law. We apply this approach to two distinct cool phases of wind in M82, the cold molecular phase and the warm neutral phase, and compare their results systematically.

Our best-fitting model has an edge-on orientation and bi-conical geometry for the outflow in M82 for both phases, consistent with earlier visual analyses. The measured outflow rate of the warm neutral phase is larger than that of the cold molecular phase, but are both similar to each other and to the SFR at the order-of-magnitude level, implying a mass-loading factor of a few. Our fits further show that for both phases, the gas clouds are radiatively driven and maintain a constant cross-sectional area as they propagate out. Our model shows good overall agreement with the observations, both for the sample spectra used for the fits and for the full 2D moment maps, although several areas of tension still remain due to the simplified geometry and physics recipes adopted by our model.

Our results suggest a picture where strong magnetic fields in M82 thread the launched gas clouds and prevent them from expanding and subsequently being destroyed by Kelvin-Helmholtz instability as they move outward along their trajectories. However, this does not imply that the gas escapes from the galaxy: our best-fitting model for the cold molecular outflow in M82 suggests that it forms a galactic foun-

tain within which the bulk of the mass falls back after travelling no higher than about 5 kpc above the galactic disc. Our modelling also shows that it is misleading to attempt to separate wind material from bound gas simply by imposing a hard velocity cutoff in observed spectra, without formulating a physically self-consistent model for the background gravitational potential and clouds' evolution along their trajectories. There is an extremely poor correspondence between the mass outflow rates we deduce from physical models and those one would obtain simply by attempting to measure the mass at any given height that is observed to be instantaneously travelling above the local escape speed.

5.2 Future work

In the future, we will self-consistently couple the rotation of outflow into our model and constrain its properties. We have already come up with the theoretical framework describing this phenomenon and have presented it in the appendix.

how to extend the model to include rotation in the outflow

A.1 Coordinate transformations

We consider the same basic setup as in Krumholz et al. [2017b, hereafter KTOM17], but now we suppose that the wind material is launched with dimensionless specific angular momentum j about the central axis of the wind, which is conserved as fluid elements flow outward. The wind central axis is oriented at an angle ϕ_a relative to the plane of the sky¹, i.e., $\phi_a = 0$ corresponds to the central wind axis being in the plane of the sky, $\phi_a = \pi/2$ to the wind axis pointing directly at the observer. The unit system in which we work is the same as used in the main paper, i.e., positions are measured in units such that the radius r_0 from which the wind is launched is unity, and velocities are measured in units such that a dimensional velocity $v = \sqrt{GM_0/r_0}$ corresponds to a dimensionless velocity of unity; here M_0 is the mass interior to r_0 . Thus $j = 1$ corresponds to a dimensional specific angular momentum $\sqrt{GM_0 r_0}$. We assume that j is small enough so that the radial velocity is always dominated by that imparted by whatever mechanism launches the wind, i.e., the contribution of rotation to the radial velocity is negligible, but that its contribution to the angular velocity (which is otherwise zero) is not. This cannot strictly be true near the wind launch point, where the wind radial velocity is zero, but will quickly become true once the wind accelerates to speeds significantly larger than the initial rotation speed. Our goal here is to compute how the line of sight velocity of the wind is affected when $j \neq 0$.

First consider the case $\phi_a = 0$, so that the wind central axis lies in the plane of the sky. In order to compute the line-of-sight velocity, we must consider transformations between several coordinate systems. The first of these is our observer-centric coordinate system described by coordinates (a, ϖ_a, ϖ_t) , where a is the 3D radial distance from the centre of the wind (in dimensionless units), ϖ_a is the impact parameter between the observer's line of sight and the wind centre, projected in the direction along the wind axis, and ϖ_t is the impact parameter of the line of sight projected

¹Note that we use ϕ_a here, rather than ϕ as in the original paper, because below we shall introduce the usual spherical coordinate ϕ , and we wish to avoid confusion between the two.

transverse to the wind axis. Our second coordinate system is a standard Cartesian coordinate system, with its origin at the centre of the wind, the z axis along the central axis of the wind, and the observer located at $y = -\infty$, so the observer's line of sight is parallel to the y axis. The coordinates in this coordinate system are related to our observer-centric one by

$$x = \omega_t \quad (\text{A.1})$$

$$y = \pm \sqrt{a^2 - \omega_a^2 - \omega_t^2} \quad (\text{A.2})$$

$$z = \omega_a. \quad (\text{A.3})$$

Finally, our third coordinate system is a standard cylindrical coordinate system, with the same origin as the Cartesian one, rotated to that the wind axis is aligned with the North pole, and $\phi = 0$ corresponds to the plane of the sky. The coordinates in this coordinate system are related to the other two by

$$r = \sqrt{x^2 + y^2} = \sqrt{a^2 - \omega_a^2} \quad (\text{A.4})$$

$$\phi = \tan^{-1} \frac{y}{x} = \tan^{-1} \sqrt{\frac{a^2}{\omega_a^2} - \frac{\omega_t^2}{\omega_a^2} - 1} \quad (\text{A.5})$$

$$z = \omega_a. \quad (\text{A.6})$$

With these coordinate systems established, and under the assumption that rotation contributes significantly only to the angular component of the velocity, we can write the vector velocity at any position as

$$\mathbf{u} = u_a \hat{a} + \frac{j}{r} \hat{\phi}, \quad (\text{A.7})$$

where u_a is the (spherical) radial velocity of the wind, \hat{a} is a unit vector in the a direction, $\hat{\phi}$ is a unit vector in the ϕ direction, and our expression makes use of our assumption that j is constant. The line-of-sight velocity is

$$u = \mathbf{u} \cdot \hat{y}. \quad (\text{A.8})$$

We can evaluate the dot product using the usual transformation rules between spherical, cylindrical, and Cartesian coordinates, whereby

$$\hat{a} \cdot \hat{y} = \frac{y}{x} \sqrt{\frac{1 - z^2/a^2}{1 + y^2/x^2}} \quad (\text{A.9})$$

$$\hat{a} \cdot \hat{\phi} = \frac{x}{\sqrt{x^2 + y^2}}. \quad (\text{A.10})$$

Substituting to replace the Cartesian coordinates by the observer-centric ones, this

gives

$$u = \pm u_a \sqrt{1 - \frac{\omega^2}{a^2}} + j \frac{\omega_t}{a^2 - \omega_a^2}, \quad (\text{A.11})$$

where $\omega^2 \equiv \omega_a^2 + \omega_t^2$, and the plus sign applies for $y > 0$ and the minus sign for $y < 0$, i.e., on the near and far sides of the wind, respectively. The first term is identical to that derived in the original paper, while the second term incorporates the effects of $j \neq 0$.

We can generalise to the case $\phi_a \neq 0$ simply by noticing that the effect of such a rotation is simply to incline the extra velocity vector $(j/r)\hat{\phi}$ relative to the line of sight, so that the amount that is projected along the line of sight is reduced by a factor $\cos \phi_a$. Thus the general relationship between u , u_a , and j is given by

$$u = \pm u_a \sqrt{1 - \frac{\omega^2}{a^2}} + j \frac{\omega_t}{a^2 - \omega_a^2} \cos \phi_a. \quad (\text{A.12})$$

A.2 Effect on observables

We now calculate the effect of this velocity shift on various observable quantities. In order to do so, we follow the same method as in KTOM17, whereby we first write the total density of material at a given position as an integral over the radial velocity distribution of the material, u_a . This is (equation 25 of KTOM17)

$$n_X = \frac{1}{m_X} \int_0^\infty \sum_i \frac{d\rho_{\text{mean}}/dx}{|dU_a/dx|} du_a, \quad (\text{A.13})$$

where ρ_{mean} is the mean density of material at distance a from the wind centre, x is the normalised column density of the material at the point where it was launched into the wind, and $u_a = U_a(x)$ describes the acceleration law for material with starting density x ; the summation is to be evaluated at all overdensities x_i that satisfy $u_a = U_a(x_i)$. The next step in KTOM17 is to make a change of variables from u_a to u , i.e., from radial to line-of-sight velocity. However, note from Equation [equation][12][A]A.12 that

$$\frac{du}{du_a} = \sqrt{1 - \frac{\omega^2}{a^2}} \quad (\text{A.14})$$

independent of j . Since the form of the differential density of absorbers at velocity u depends only on du/du_a , this is unchanged from the form given in equation (29) of KTOM17, i.e., the differential density of particles of species X with line of sight velocities in the infinitesimal interval u to $u + du$ is

$$\frac{dn_X}{du} = \frac{1}{m_X} \frac{a}{\sqrt{a^2 - \omega_a^2}} \sum_i \frac{d\rho_{\text{mean}}/dx}{|dU_a/dx|}. \quad (\text{A.15})$$

The effect of rotation appears only in the values x_i at which the summation is evaluated, which are now given implicitly by

$$U_a(x_i) = \pm \frac{a}{\sqrt{a^2 - \omega^2}} \left(u - j \frac{\omega_t}{a^2 - \omega_a^2} \cos \phi_a \right), \quad (\text{A.16})$$

where the plus sign appears for the far side of the wind and the minus sign for the near side. For $j = 0$, this reduces to equation (28) of KTOM17.

There is, however, an important conceptual difference between the cases $j = 0$ and $j \neq 0$. For $j = 0$, for each u solutions exist only on the near or far side of the wind regardless of the value of a ; that is, if $u > 0$, then since U_a is a strictly positive function, solutions x_i exist only if we select the positive root in Equation [equation][16][A]A.16, and thus are on the far side of the wind. Similarly, $u < 0$ implies solutions only on the near side. For $j \neq 0$ the situation is somewhat more complex, because on which side of the wind a given solution exists does depend on a . Specifically, for a given combination of u , a , and j , a solution can exist on the far side of the wind (positive root) only if

$$u - j \frac{\omega_t}{a^2 - \omega_a^2} \cos \phi_a > 0, \quad (\text{A.17})$$

with an identical condition except for a reverse inequality for a solution to exist on the near side of the wind. Thus for some combinations of u , ω_a , and ω_t , solutions exist only on one side of the wind, while for other combinations solutions exist on both sides. Specifically, note that the second term on the left hand side of Equation [equation][17][A]A.17 reaches its maximum absolute value when $a^2 = \omega_t^2 + \omega_a^2$, at which point this term takes on a value $u_{\text{rot,max}} = (j/\omega_t) \cos \phi_a$. We can therefore say that solutions on both sides of the wind are possible only if

$$\begin{aligned} 0 < u < u_{\text{rot,max}} & \quad \text{if} \quad u_{\text{rot,max}} > 0 \\ u_{\text{rot,max}} < u < 0 & \quad \text{if} \quad u_{\text{rot,max}} < 0. \end{aligned} \quad (\text{A.18})$$

Note that this is a necessary but not a sufficient condition; whether solutions in fact exist on both sides depends on the function $U_a(x)$.

Bibliography

- ALATALO, K.; BLITZ, L.; YOUNG, L. M.; DAVIS, T. A.; BUREAU, M.; LOPEZ, L. A.; CAPPELLARI, M.; SCOTT, N.; SHAPIRO, K. L.; CROCKER, A. F.; MARTÍN, S.; BOIS, M.; BOURNAUD, F.; DAVIES, R. L.; DE ZEEUW, P. T.; DUC, P. A.; Emsellem, E.; Falcón-Barroso, J.; KHOCHFAR, S.; KRAJNOVIĆ, D.; KUNTSCHNER, H.; LABLANCHE, P. Y.; McDERMID, R. M.; MORGANTI, R.; NAAB, T.; OOSTERLOO, T.; SARZI, M.; SERRA, P.; AND WEIJMANS, A., 2011. Discovery of an Active Galactic Nucleus Driven Molecular Outflow in the Local Early-type Galaxy NGC 1266. *ApJ*, 735, 2 (Jul. 2011), 88. doi:10.1088/0004-637X/735/2/88. (cited on page 6)
- BACCHINI, C.; FRATERNALI, F.; IORIO, G.; PEZZULLI, G.; MARASCO, A.; AND NIPOTI, C., 2020. Evidence for supernova feedback sustaining gas turbulence in nearby star-forming galaxies. *A&A*, 641 (Sep. 2020), A70. doi:10.1051/0004-6361/202038223. (cited on page 4)
- BANDA-BARRAGÁN, W. E.; FEDERRATH, C.; CROCKER, R. M.; AND BICKNELL, G. V., 2018. Filament formation in wind-cloud interactions- II. Clouds with turbulent density, velocity, and magnetic fields. *MNRAS*, 473, 3 (Jan. 2018), 3454–3489. doi:10.1093/mnras/stx2541. (cited on page 35)
- BANDA-BARRAGÁN, W. E.; ZERTUCHE, F. J.; FEDERRATH, C.; GARCÍA DEL VALLE, J.; BRÜGGEN, M.; AND WAGNER, A. Y., 2019. On the dynamics and survival of fractal clouds in galactic winds. *MNRAS*, 486, 4 (Jul. 2019), 4526–4544. doi:10.1093/mnras/stz1040. (cited on page 3)
- BREGMAN, J. N., 1980. The galactic fountain of high-velocity clouds. *ApJ*, 236 (Mar. 1980), 577–591. doi:10.1086/157776. (cited on page 4)
- BREGMAN, J. N.; SCHULMAN, E.; AND TOMISAKA, K., 1995. High-Resolution X-Ray Imaging of the Starburst Galaxy M82. *ApJ*, 439 (Jan. 1995), 155. doi:10.1086/175160. (cited on page 11)
- BUCKMAN, B. J.; LINDEN, T.; AND THOMPSON, T. A., 2020. Cosmic rays and magnetic fields in the core and halo of the starburst M82: implications for galactic wind physics. *MNRAS*, 494, 2 (Apr. 2020), 2679–2705. doi:10.1093/mnras/staa875. (cited on page 36)
- CARR, C.; SCARLATA, C.; PANAGIA, N.; AND HENRY, A., 2018. A Semi-analytical Line Transfer (SALT) Model. II: The Effects of a Bi-conical Geometry. *ApJ*, 860, 2 (Jun. 2018), 143. doi:10.3847/1538-4357/aac48e. (cited on page 7)

-
- CHABRIER, G., 2005. *The Initial Mass Function: From Salpeter 1955 to 2005*, vol. 327, 41. doi:10.1007/978-1-4020-3407-7_5. (cited on page 19)
- CHEVALIER, R. A. AND CLEGG, A. W., 1985. Wind from a starburst galaxy nucleus. *Nature*, 317, 6032 (Sep. 1985), 44–45. doi:10.1038/317044a0. (cited on page 3)
- COSTA, T.; ROSDAHL, J.; SIJACKI, D.; AND HAEHNELT, M. G., 2018. Driving gas shells with radiation pressure on dust in radiation-hydrodynamic simulations. *MNRAS*, 473, 3 (Jan. 2018), 4197–4219. doi:10.1093/mnras/stx2598. (cited on page 13)
- COSTA, T.; SIJACKI, D.; AND HAEHNELT, M. G., 2014. Feedback from active galactic nuclei: energy- versus momentum-driving. *MNRAS*, 444, 3 (Nov. 2014), 2355–2376. doi:10.1093/mnras/stu1632. (cited on page 12)
- COSTA, T.; SIJACKI, D.; AND HAEHNELT, M. G., 2015. Fast cold gas in hot AGN outflows. *MNRAS*, 448 (Mar. 2015), L30–L34. doi:10.1093/mnrasl/slu193. (cited on page 12)
- COTTLE, J.; SCANNAPIECO, E.; BRÜGGEN, M.; BANDA-BARRAGÁN, W.; AND FEDERRATH, C., 2020. The Launching of Cold Clouds by Galaxy Outflows. III. The Influence of Magnetic Fields. *ApJ*, 892, 1 (Mar. 2020), 59. doi:10.3847/1538-4357/ab76d1. (cited on page 3)
- FIELDING, D. B.; OSTRICKER, E. C.; BRYAN, G. L.; AND JERMYN, A. S., 2020. Multiphase Gas and the Fractal Nature of Radiative Turbulent Mixing Layers. *ApJ*, 894, 2 (May 2020), L24. doi:10.3847/2041-8213/ab8d2c. (cited on page 3)
- FLUETSCH, A.; MAIOLINO, R.; CARNIANI, S.; MARCONI, A.; CICONE, C.; BOURNE, M. A.; COSTA, T.; FABIAN, A. C.; ISHIBASHI, W.; AND VENTURI, G., 2019. Cold molecular outflows in the local Universe and their feedback effect on galaxies. *MNRAS*, 483, 4 (Mar. 2019), 4586–4614. doi:10.1093/mnras/sty3449. (cited on page 17)
- FOREMAN-MACKEY, D.; HOGG, D. W.; LANG, D.; AND GOODMAN, J., 2013. emcee: The MCMC Hammer. *PASP*, 125, 925 (Mar. 2013), 306. doi:10.1086/670067. (cited on page 17)
- FREEDMAN, W. L.; HUGHES, S. M.; MADORE, B. F.; MOULD, J. R.; LEE, M. G.; STETSON, P.; KENNICUTT, R. C.; TURNER, A.; FERRARESE, L.; FORD, H.; GRAHAM, J. A.; HILL, R.; HOESSEL, J. G.; HUCHRA, J.; AND ILLINGWORTH, G. D., 1994. The Hubble Space Telescope Extragalactic Distance Scale Key Project. I. The Discovery of Cepheids and a New Distance to M81. *ApJ*, 427 (Jun. 1994), 628. doi:10.1086/174172. (cited on page 9)
- GALLEGOS-GARCIA, M.; BURKHART, B.; ROSEN, A. L.; NAIMAN, J. P.; AND RAMIREZ-RUIZ, E., 2020. Winds in Star Clusters Drive Kolmogorov Turbulence. *ApJ*, 899, 2 (Aug. 2020), L30. doi:10.3847/2041-8213/ababae. (cited on page 4)

-
- GENTRY, E. S.; KRUMHOLZ, M. R.; MADAU, P.; AND LUPI, A., 2019. The momentum budget of clustered supernova feedback in a 3D, magnetized medium. *MNRAS*, 483, 3 (Mar. 2019), 3647–3658. doi:10.1093/mnras/sty3319. (cited on page 36)
- GENZEL, R.; NEWMAN, S.; JONES, T.; FÖRSTER SCHREIBER, N. M.; SHAPIRO, K.; GENEL, S.; LILLY, S. J.; RENZINI, A.; TACCONI, L. J.; BOUCHÉ, N.; BURKERT, A.; CRESCI, G.; BUSCHKAMP, P.; CAROLLO, C. M.; CEVERINO, D.; DAVIES, R.; DEKEL, A.; EISENHAUER, F.; HICKS, E.; KURK, J.; LUTZ, D.; MANCINI, C.; NAAB, T.; PENG, Y.; STERNBERG, A.; VERGANI, D.; AND ZAMORANI, G., 2011. The Sins Survey of $z \sim 2$ Galaxy Kinematics: Properties of the Giant Star-forming Clumps. *ApJ*, 733, 2 (Jun. 2011), 101. doi:10.1088/0004-637X/733/2/101. (cited on page 6)
- GRECO, J. P.; MARTINI, P.; AND THOMPSON, T. A., 2012. Measurement of the Mass and Stellar Population Distribution in M82 with the LBT. *ApJ*, 757, 1 (Sep. 2012), 24. doi:10.1088/0004-637X/757/1/24. (cited on page 19)
- GREVE, A., 2004. The rotating visible outflow in M 82. *A&A*, 416 (Mar. 2004), 67–78. doi:10.1051/0004-6361:20031709. (cited on page 16)
- GRONKE, M. AND OH, S. P., 2018. The growth and entrainment of cold gas in a hot wind. *MNRAS*, 480, 1 (Oct. 2018), L111–L115. doi:10.1093/mnras/sly131. (cited on page 3)
- GRONKE, M. AND OH, S. P., 2020. How cold gas continuously entrains mass and momentum from a hot wind. *MNRAS*, 492, 2 (Feb. 2020), 1970–1990. doi:10.1093/mnras/stz3332. (cited on page 3)
- GRØNNOW, A.; TEPPER-GARCÍA, T.; BLAND-HAWTHORN, J.; AND MCCLURE-GRIFFITHS, N. M., 2017. Magnetized High Velocity Clouds in the Galactic Halo: A New Distance Constraint. *ApJ*, 845, 1 (Aug. 2017), 69. doi:10.3847/1538-4357/aa7ed2. (cited on page 36)
- HECKMAN, T. M.; ARMUS, L.; AND MILEY, G. K., 1990. On the Nature and Implications of Starburst-driven Galactic Superwinds. *ApJS*, 74 (Dec. 1990), 833. doi:10.1086/191522. (cited on pages xiii, 5, and 6)
- HECKMAN, T. M.; LEHNERT, M. D.; STRICKLAND, D. K.; AND ARMUS, L., 2000. Absorption-Line Probes of Gas and Dust in Galactic Superwinds. *ApJS*, 129, 2 (Aug. 2000), 493–516. doi:10.1086/313421. (cited on page 6)
- HECKMAN, T. M. AND THOMPSON, T. A., 2017. Galactic Winds and the Role Played by Massive Stars. *arXiv e-prints*, (Jan. 2017), arXiv:1701.09062. (cited on page 1)
- HOOPES, C. G.; HECKMAN, T. M.; STRICKLAND, D. K.; AND HOWK, J. C., 2003. Cooling in Coronal Gas in the M82 Starburst Superwind. *ApJ*, 596, 2 (Oct. 2003), L175–L178. doi:10.1086/379533. (cited on page 38)

-
- HOPKINS, P. F. AND ELVIS, M., 2010. Quasar feedback: more bang for your buck. *MNRAS*, 401, 1 (Jan. 2010), 7–14. doi:10.1111/j.1365-2966.2009.15643.x. (cited on page 35)
- HOPKINS, P. F.; KEREŠ, D.; OÑORBE, J.; FAUCHER-GIGUÈRE, C.-A.; QUATAERT, E.; MURRAY, N.; AND BULLOCK, J. S., 2014. Galaxies on FIRE (Feedback In Realistic Environments): stellar feedback explains cosmologically inefficient star formation. *MNRAS*, 445, 1 (Nov. 2014), 581–603. doi:10.1093/mnras/stu1738. (cited on page 4)
- HOPKINS, P. F.; QUATAERT, E.; AND MURRAY, N., 2011. Self-regulated star formation in galaxies via momentum input from massive stars. *MNRAS*, 417, 2 (Oct. 2011), 950–973. doi:10.1111/j.1365-2966.2011.19306.x. (cited on page 4)
- HOPKINS, P. F.; QUATAERT, E.; AND MURRAY, N., 2012. Stellar feedback in galaxies and the origin of galaxy-scale winds. *MNRAS*, 421, 4 (Apr. 2012), 3522–3537. doi:10.1111/j.1365-2966.2012.20593.x. (cited on page 2)
- JANSSEN, A. W.; CHRISTOPHER, N.; STURM, E.; VEILLEUX, S.; CONTURSI, A.; GONZÁLEZ-ALFONSO, E.; FISCHER, J.; DAVIES, R.; VERMA, A.; GRACIÁ-CARPIO, J.; GENZEL, R.; LUTZ, D.; STERNBERG, A.; TACCONI, L.; BURTSCHER, L.; AND POGLITSCH, A., 2016. Broad [C II] Line Wings as Tracer of Molecular and Multi-phase Outflows in Infrared Bright Galaxies. *ApJ*, 822, 1 (May 2016), 43. doi:10.3847/0004-637X/822/1/43. (cited on page 6)
- Ji, S.; OH, S. P.; AND MASTERSON, P., 2019. Simulations of radiative turbulent mixing layers. *MNRAS*, 487, 1 (Jul. 2019), 737–754. doi:10.1093/mnras/stz1248. (cited on page 3)
- JONES, T. J.; DOWELL, C. D.; LOPEZ RODRIGUEZ, E.; ZWEIBEL, E. G.; BERTHOUD, M.; CHUSS, D. T.; GOLDSMITH, P. F.; HAMILTON, R. T.; HANANY, S.; HARPER, D. A.; LAZARIAN, A.; LOONEY, L. W.; MICHAIL, J. M.; MORRIS, M. R.; NOVAK, G.; SANTOS, F. P.; SHETH, K.; STACEY, G. J.; STAGUHN, J.; STEPHENS, I. W.; TASSIS, K.; TRINH, C. Q.; VOLPERT, C. G.; WERNER, M.; WOLLACK, E. J.; AND HAWC+ SCIENCE TEAM, 2019. SOFIA Far-infrared Imaging Polarimetry of M82 and NGC 253: Exploring the Supergalactic Wind. *ApJ*, 870, 1 (Jan. 2019), L9. doi:10.3847/2041-8213/aaf8b9. (cited on page 36)
- KENNICUTT, J., ROBERT C., 1998. The Global Schmidt Law in Star-forming Galaxies. *ApJ*, 498, 2 (May 1998), 541–552. doi:10.1086/305588. (cited on page 19)
- KIM, J.-G.; KIM, W.-T.; AND OSTRICKER, E. C., 2018. Modeling UV Radiation Feedback from Massive Stars. II. Dispersal of Star-forming Giant Molecular Clouds by Photoionization and Radiation Pressure. *ApJ*, 859, 1 (May 2018), 68. doi:10.3847/1538-4357/aabe27. (cited on page 4)

-
- KRUMHOLZ, M. R., 2014. DESPOTIC - a new software library to Derive the Energetics and SPectra of Optically Thick Interstellar Clouds. *MNRAS*, 437, 2 (Jan. 2014), 1662–1680. doi:10.1093/mnras/stt2000. (cited on page 8)
- KRUMHOLZ, M. R. AND BURKHART, B., 2016. Is turbulence in the interstellar medium driven by feedback or gravity? An observational test. *MNRAS*, 458, 2 (May 2016), 1671–1677. doi:10.1093/mnras/stw434. (cited on page 4)
- KRUMHOLZ, M. R.; BURKHART, B.; FORBES, J. C.; AND CROCKER, R. M., 2018. A unified model for galactic discs: star formation, turbulence driving, and mass transport. *MNRAS*, 477, 2 (Jun. 2018), 2716–2740. doi:10.1093/mnras/sty852. (cited on page 4)
- KRUMHOLZ, M. R.; KRUIJSSEN, J. M. D.; AND CROCKER, R. M., 2017a. A dynamical model for gas flows, star formation and nuclear winds in galactic centres. *MNRAS*, 466, 1 (Apr. 2017), 1213–1233. doi:10.1093/mnras/stw3195. (cited on page 12)
- KRUMHOLZ, M. R. AND THOMPSON, T. A., 2013. Numerical simulations of radiatively driven dusty winds. *MNRAS*, 434, 3 (Sep. 2013), 2329–2346. doi:10.1093/mnras/stt1174. (cited on pages 3 and 13)
- KRUMHOLZ, M. R.; THOMPSON, T. A.; OSTRICKER, E. C.; AND MARTIN, C. L., 2017b. The observable properties of cool winds from galaxies, AGN, and star clusters - I. Theoretical framework. *MNRAS*, 471, 4 (Nov. 2017), 4061–4086. doi:10.1093/mnras/stx1882. (cited on pages xvii, 8, 11, 12, 13, 15, 19, 36, 43, 45, and 46)
- LEROY, A. K.; WALTER, F.; MARTINI, P.; ROUSSEL, H.; SANDSTROM, K.; OTT, J.; WEISS, A.; BOLATTO, A. D.; SCHUSTER, K.; AND DESSAUGES-ZAVADSKY, M., 2015. The Multi-phase Cold Fountain in M82 Revealed by a Wide, Sensitive Map of the Molecular Interstellar Medium. *ApJ*, 814, 2 (Dec. 2015), 83. doi:10.1088/0004-637X/814/2/83. (cited on pages xiii, 6, 10, 11, 19, and 30)
- LI, M. AND TONNESEN, S., 2020. How Do Supernovae Impact the Circumgalactic Medium? I. Large-scale Fountains around a Milky Way-like Galaxy. *ApJ*, 898, 2 (Aug. 2020), 148. doi:10.3847/1538-4357/ab9f9f. (cited on page 4)
- LI, Z.; HOPKINS, P. F.; SQUIRE, J.; AND HUMMELS, C., 2020. On the survival of cool clouds in the circumgalactic medium. *MNRAS*, 492, 2 (Feb. 2020), 1841–1854. doi:10.1093/mnras/stz3567. (cited on page 3)
- LOCHHAAS, C.; THOMPSON, T. A.; QUATAERT, E.; AND WEINBERG, D. H., 2018. Fast winds drive slow shells: a model for the circumgalactic medium as galactic wind-driven bubbles. *MNRAS*, 481, 2 (Dec. 2018), 1873–1896. doi:10.1093/mnras/sty2421. (cited on page 7)
- LOPEZ, L. A.; MATHUR, S.; NGUYEN, D. D.; THOMPSON, T. A.; AND OLIVIER, G. M., 2020. Temperature and Metallicity Gradients in the Hot Gas Outflows of M82. *ApJ*, 904, 2 (Dec. 2020), 152. doi:10.3847/1538-4357/abc010. (cited on page 11)

-
- LOPEZ-RODRIGUEZ, E.; GUERRA, J.; ASGARI-TARGHI, M.; AND SCHMELZ, J. T., 2021. The strength and structure of the magnetic field in the galactic outflow of M82. *arXiv e-prints*, (Feb. 2021), arXiv:2102.03362. (cited on page 36)
- LYNDS, C. R. AND SANDAGE, A. R., 1963. Evidence for an Explosion in the Center of the Galaxy M82. *ApJ*, 137 (May 1963), 1005. doi:10.1086/147579. (cited on page 1)
- MARASCO, A. AND FRATERNALI, F., 2017. The Galactic fountain as an origin for the Smith Cloud. *MNRAS*, 464, 1 (Jan. 2017), L100–L104. doi:10.1093/mnrasl/slw195. (cited on page 4)
- MARTIN, C. L., 1998. The Impact of Star Formation on the Interstellar Medium in Dwarf Galaxies. II. The Formation of Galactic Winds. *ApJ*, 506, 1 (Oct. 1998), 222–252. doi:10.1086/306219. (cited on page 11)
- MARTIN, C. L., 2005. Mapping Large-Scale Gaseous Outflows in Ultraluminous Galaxies with Keck II ESI Spectra: Variations in Outflow Velocity with Galactic Mass. *ApJ*, 621, 1 (Mar. 2005), 227–245. doi:10.1086/427277. (cited on page 6)
- MARTINI, P.; LEROY, A. K.; MANGUM, J. G.; BOLATTO, A.; KEATING, K. M.; SANDSTROM, K.; AND WALTER, F., 2018. H I Kinematics along the Minor Axis of M82. *ApJ*, 856, 1 (Mar. 2018), 61. doi:10.3847/1538-4357/aab08e. (cited on pages xiii, 10, 11, 19, 20, and 39)
- MCCOURT, M.; O’LEARY, R. M.; MADIGAN, A.-M.; AND QUATAERT, E., 2015. Magnetized gas clouds can survive acceleration by a hot wind. *MNRAS*, 449, 1 (May 2015), 2–7. doi:10.1093/mnras/stv355. (cited on pages 3 and 35)
- MCKEITH, C. D.; GREVE, A.; DOWNES, D.; AND PRADA, F., 1995. The outflow in the halo of M 82. *A&A*, 293 (Jan. 1995), 703–709. (cited on page 11)
- MELIOLI, C.; BRIGHENTI, F.; AND D’ERCOLE, A., 2015. Galactic fountains and outflows in star-forming dwarf galaxies: interstellar medium expulsion and chemical enrichment. *MNRAS*, 446, 1 (Jan. 2015), 299–316. doi:10.1093/mnras/stu2008. (cited on page 4)
- MURATOV, A. L.; KEREŠ, D.; FAUCHER-GIGUÈRE, C.-A.; HOPKINS, P. F.; MA, X.; ANGLÉS-ALCÁZAR, D.; CHAN, T. K.; TORREY, P.; HAFEN, Z. H.; QUATAERT, E.; AND MURRAY, N., 2017. Metal flows of the circumgalactic medium, and the metal budget in galactic haloes. *MNRAS*, 468, 4 (Jul. 2017), 4170–4188. doi:10.1093/mnras/stx667. (cited on page 4)
- MURATOV, A. L.; KEREŠ, D.; FAUCHER-GIGUÈRE, C.-A.; HOPKINS, P. F.; QUATAERT, E.; AND MURRAY, N., 2015. Gusty, gaseous flows of FIRE: galactic winds in cosmological simulations with explicit stellar feedback. *MNRAS*, 454, 3 (Dec. 2015), 2691–2713. doi:10.1093/mnras/stv2126. (cited on page 17)

-
- MURRAY, N.; QUATAERT, E.; AND THOMPSON, T. A., 2005. On the Maximum Luminosity of Galaxies and Their Central Black Holes: Feedback from Momentum-driven Winds. *ApJ*, 618, 2 (Jan. 2005), 569–585. doi:10.1086/426067. (cited on page 4)
- NELSON, D.; KAUFFMANN, G.; PILLEPICH, A.; GENEL, S.; SPRINGEL, V.; PAKMOR, R.; HERNQUIST, L.; WEINBERGER, R.; TORREY, P.; VOGELSBERGER, M.; AND MARINACCI, F., 2018. The abundance, distribution, and physical nature of highly ionized oxygen O VI, O VII, and O VIII in IllustrisTNG. *MNRAS*, 477, 1 (Jun. 2018), 450–479. doi:10.1093/mnras/sty656. (cited on page 4)
- NELSON, D.; PILLEPICH, A.; SPRINGEL, V.; PAKMOR, R.; WEINBERGER, R.; GENEL, S.; TORREY, P.; VOGELSBERGER, M.; MARINACCI, F.; AND HERNQUIST, L., 2019. First results from the TNG50 simulation: galactic outflows driven by supernovae and black hole feedback. *MNRAS*, 490, 3 (Dec. 2019), 3234–3261. doi:10.1093/mnras/stz2306. (cited on pages 2 and 12)
- O’CONNELL, R. W.; GALLAGHER, I.; JOHN S.; HUNTER, D. A.; AND COLLEY, W. N., 1995. Hubble Space Telescope Imaging of Super Star Clusters in M82. *ApJ*, 446 (Jun. 1995), L1. doi:10.1086/187916. (cited on page 9)
- O’CONNELL, R. W. AND MANGANO, J. J., 1978. The central regions of M82. *ApJ*, 221 (Apr. 1978), 62–79. doi:10.1086/156005. (cited on page 9)
- OPPENHEIMER, B. D. AND DAVÉ, R., 2006. Cosmological simulations of intergalactic medium enrichment from galactic outflows. *MNRAS*, 373, 4 (Dec. 2006), 1265–1292. doi:10.1111/j.1365-2966.2006.10989.x. (cited on page 4)
- PETTINI, M.; RIX, S. A.; STEIDEL, C. C.; ADELBERGER, K. L.; HUNT, M. P.; AND SHAPLEY, A. E., 2002. New Observations of the Interstellar Medium in the Lyman Break Galaxy MS 1512-cB58. *ApJ*, 569, 2 (Apr. 2002), 742–757. doi:10.1086/339355. (cited on pages xiii, 6, and 7)
- PROCHASKA, J. X.; KASEN, D.; AND RUBIN, K., 2011. Simple Models of Metal-line Absorption and Emission from Cool Gas Outflows. *ApJ*, 734, 1 (Jun. 2011), 24. doi:10.1088/0004-637X/734/1/24. (cited on pages 6 and 7)
- ROBERTS-BORSANI, G. W., 2020. Observational constraints on the multiphase nature of outflows using large spectroscopic surveys at $z \sim 0$. *MNRAS*, 494, 3 (Apr. 2020), 4266–4278. doi:10.1093/mnras/staa1006. (cited on page 17)
- ROBERTS-BORSANI, G. W. AND SAINTONGE, A., 2019. The prevalence and properties of cold gas inflows and outflows around galaxies in the local Universe. *MNRAS*, 482, 3 (Jan. 2019), 4111–4145. doi:10.1093/mnras/sty2824. (cited on page 17)
- ROBERTS-BORSANI, G. W.; SAINTONGE, A.; MASTERS, K. L.; AND STARK, D. V., 2020. Outflows in star-forming galaxies: Stacking analyses of resolved winds and the relation to their hosts’ properties. *MNRAS*, 493, 3 (Apr. 2020), 3081–3097. doi:10.1093/mnras/staa464. (cited on page 17)

-
- RUPKE, D. S.; VEILLEUX, S.; AND SANDERS, D. B., 2005a. Outflows in Infrared-Luminous Starbursts at $z < 0.5$. I. Sample, Na I D Spectra, and Profile Fitting. *ApJS*, 160, 1 (Sep. 2005), 87–114. doi:10.1086/432886. (cited on page 6)
- RUPKE, D. S.; VEILLEUX, S.; AND SANDERS, D. B., 2005b. Outflows in Infrared-Luminous Starbursts at $z < 0.5$. II. Analysis and Discussion. *ApJS*, 160, 1 (Sep. 2005), 115–148. doi:10.1086/432889. (cited on page 6)
- SCANNAPIECO, E. AND BRÜGGEN, M., 2015. The Launching of Cold Clouds by Galaxy Outflows. I. Hydrodynamic Interactions with Radiative Cooling. *ApJ*, 805, 2 (Jun. 2015), 158. doi:10.1088/0004-637X/805/2/158. (cited on page 3)
- SCARLATA, C. AND PANAGIA, N., 2015. A Semi-analytical Line Transfer Model to Interpret the Spectra of Galaxy Outflows. *ApJ*, 801, 1 (Mar. 2015), 43. doi:10.1088/0004-637X/801/1/43. (cited on page 7)
- SCHNEIDER, E. E.; ROBERTSON, B. E.; AND THOMPSON, T. A., 2018. Production of Cool Gas in Thermally Driven Outflows. *ApJ*, 862, 1 (Jul. 2018), 56. doi:10.3847/1538-4357/aacce1. (cited on pages xiii, 2, and 3)
- SHARMA, S., 2017. Markov Chain Monte Carlo Methods for Bayesian Data Analysis in Astronomy. *ARA&A*, 55, 1 (Aug. 2017), 213–259. doi:10.1146/annurev-astro-082214-122339. (cited on page 18)
- SHOPBELL, P. L. AND BLAND-HAWTHORN, J., 1998. The Asymmetric Wind in M82. *ApJ*, 493, 1 (Jan. 1998), 129–153. doi:10.1086/305108. (cited on pages 11 and 14)
- SMITH, M. C.; BRYAN, G. L.; SOMERVILLE, R. S.; HU, C.-Y.; TEYSSIER, R.; BURKHART, B.; AND HERNQUIST, L., 2020. Efficient early stellar feedback can suppress galactic outflows by reducing supernova clustering. *arXiv e-prints*, (Sep. 2020), arXiv:2009.11309. (cited on page 2)
- SPRINGEL, V. AND HERNQUIST, L., 2003. Cosmological smoothed particle hydrodynamics simulations: a hybrid multiphase model for star formation. *MNRAS*, 339, 2 (Feb. 2003), 289–311. doi:10.1046/j.1365-8711.2003.06206.x. (cited on page 4)
- STEIDEL, C. C.; ERB, D. K.; SHAPLEY, A. E.; PETTINI, M.; REDDY, N.; BOGOSAVLJEVIĆ, M.; RUDIE, G. C.; AND RAKIC, O., 2010. The Structure and Kinematics of the Circumgalactic Medium from Far-ultraviolet Spectra of $z \sim 2$ –3 Galaxies. *ApJ*, 717, 1 (Jul. 2010), 289–322. doi:10.1088/0004-637X/717/1/289. (cited on pages 6 and 7)
- STRICKLAND, D. K. AND HECKMAN, T. M., 2009. Supernova Feedback Efficiency and Mass Loading in the Starburst and Galactic Superwind Exemplar M82. *ApJ*, 697, 2 (Jun. 2009), 2030–2056. doi:10.1088/0004-637X/697/2/2030. (cited on page 22)
- STRICKLAND, D. K.; PONMAN, T. J.; AND STEVENS, I. R., 1997. ROSAT observations of the galactic wind in M 82. *A&A*, 320 (Apr. 1997), 378–394. (cited on page 11)

-
- TAN, B.; OH, S. P.; AND GRONKE, M., 2020. Radiative Mixing Layers: Insights from Turbulent Combustion. *arXiv e-prints*, (Aug. 2020), arXiv:2008.12302. (cited on page 3)
- THOMPSON, T. A.; FABIAN, A. C.; QUATAERT, E.; AND MURRAY, N., 2015. Dynamics of dusty radiation-pressure-driven shells and clouds: fast outflows from galaxies, star clusters, massive stars, and AGN. *MNRAS*, 449, 1 (May 2015), 147–161. doi:10.1093/mnras/stv246. (cited on page 12)
- THOMPSON, T. A. AND KRUMHOLZ, M. R., 2016. Sub-Eddington star-forming regions are super-Eddington: momentum-driven outflows from supersonic turbulence. *MNRAS*, 455, 1 (Jan. 2016), 334–342. doi:10.1093/mnras/stv2331. (cited on pages 12 and 14)
- THOMPSON, T. A.; QUATAERT, E.; AND MURRAY, N., 2005. Radiation Pressure-supported Starburst Disks and Active Galactic Nucleus Fueling. *ApJ*, 630, 1 (Sep. 2005), 167–185. doi:10.1086/431923. (cited on page 4)
- THOMPSON, T. A.; QUATAERT, E.; ZHANG, D.; AND WEINBERG, D. H., 2016. An origin for multiphase gas in galactic winds and haloes. *MNRAS*, 455, 2 (Jan. 2016), 1830–1844. doi:10.1093/mnras/stv2428. (cited on pages 3 and 35)
- TUMLINSON, J.; THOM, C.; WERK, J. K.; PROCHASKA, J. X.; TRIPP, T. M.; WEINBERG, D. H.; PEEPLES, M. S.; O’MEARA, J. M.; OPPENHEIMER, B. D.; MEIRING, J. D.; KATZ, N. S.; DAVÉ, R.; FORD, A. B.; AND SEMBACH, K. R., 2011. The Large, Oxygen-Rich Halos of Star-Forming Galaxies Are a Major Reservoir of Galactic Metals. *Science*, 334, 6058 (Nov. 2011), 948. doi:10.1126/science.1209840. (cited on page 4)
- VEILLEUX, S.; CECIL, G.; AND BLAND-HAWTHORN, J., 2005. Galactic Winds. *ARA&A*, 43, 1 (Sep. 2005), 769–826. doi:10.1146/annurev.astro.43.072103.150610. (cited on page 1)
- VEILLEUX, S.; MAIOLINO, R.; BOLATTO, A. D.; AND AALTO, S., 2020. Cool Outflows in Galaxies and their Implications. *arXiv e-prints*, (Feb. 2020), arXiv:2002.07765. (cited on page 1)
- WALTER, F.; BOLATTO, A. D.; LEROY, A. K.; VEILLEUX, S.; WARREN, S. R.; HODGE, J.; LEVY, R. C.; MEIER, D. S.; OSTRICKER, E. C.; OTT, J.; ROSOLOWSKY, E.; SCOVILLE, N.; WEISS, A.; ZSCHAECHNER, L.; AND ZWAAN, M., 2017. Dense Molecular Gas Tracers in the Outflow of the Starburst Galaxy NGC 253. *ApJ*, 835, 2 (Feb. 2017), 265. doi:10.3847/1538-4357/835/2/265. (cited on page 30)
- WALTER, F.; WEISS, A.; MARTIN, C.; AND SCOVILLE, N., 2002. The Interacting Dwarf Galaxy NGC 3077: The Interplay of Atomic and Molecular Gas with Violent Star Formation. *AJ*, 123, 1 (Jan. 2002), 225–237. doi:10.1086/324633. (cited on page 11)
- WATSON, M. G.; STANGER, V.; AND GRIFFITHS, R. E., 1984. X-ray emission from M 82. *ApJ*, 286 (Nov. 1984), 144–158. doi:10.1086/162583. (cited on page 11)

-
- WERK, J. K.; PROCHASKA, J. X.; TUMLINSON, J.; PEEPLES, M. S.; TRIPP, T. M.; FOX, A. J.; LEHNER, N.; THOM, C.; O'MEARA, J. M.; FORD, A. B.; BORDOLOI, R.; KATZ, N.; TEJOS, N.; OPPENHEIMER, B. D.; DAVÉ, R.; AND WEINBERG, D. H., 2014. The COS-Halos Survey: Physical Conditions and Baryonic Mass in the Low-redshift Circumgalactic Medium. *ApJ*, 792, 1 (Sep. 2014), 8. doi:10.1088/0004-637X/792/1/8. (cited on page 6)
- WERK, J. K.; RUBIN, K. H. R.; BISH, H. V.; PROCHASKA, J. X.; ZHENG, Y.; O'MEARA, J. M.; LENZ, D.; HUMMELS, C.; AND DEASON, A. J., 2019. The Nature of Ionized Gas in the Milky Way Galactic Fountain. *ApJ*, 887, 1 (Dec. 2019), 89. doi:10.3847/1538-4357/ab54cf. (cited on page 4)
- WESTMOQUETTE, M. S.; GALLAGHER, J. S.; SMITH, L. J.; TRANCHO, G.; BASTIAN, N.; AND KONSTANTOPOULOS, I. S., 2009. The Optical Structure of the Starburst Galaxy M82. II. Nebular Properties of the Disk and Inner Wind. *ApJ*, 706, 2 (Dec. 2009), 1571–1587. doi:10.1088/0004-637X/706/2/1571. (cited on page 11)
- WILD, W.; HARRIS, A. I.; ECKART, A.; GENZEL, R.; GRAF, U. U.; JACKSON, J. M.; RUSSELL, A. P. G.; AND STUTZKI, J., 1992. A multi-line study of the molecular interstellar medium in M 82's starburst nucleus. *A&A*, 265 (Nov. 1992), 447. (cited on page 19)
- WRIGHT, T., 1750. *An original theory or new hypothesis of the universe : founded upon general phaenomena of the visible creation; and particularly the Via the laws of nature, and solving by mathematical principles : the Lactea ...compris'd in nine familiar letters from the author to his friendand : illustrated with upward of thirty graven and mezzotinto plates ...* doi:10.3931/e-rara-28672. (cited on page 1)
- YOAST-HULL, T. M.; EVERETT, J. E.; GALLAGHER, I., J. S.; AND ZWEIBEL, E. G., 2013. Winds, Clumps, and Interacting Cosmic Rays in M82. *ApJ*, 768, 1 (May 2013), 53. doi:10.1088/0004-637X/768/1/53. (cited on page 36)
- ZHANG, D.; DAVIS, S. W.; JIANG, Y.-F.; AND STONE, J. M., 2018. Dusty Cloud Acceleration by Radiation Pressure in Rapidly Star-forming Galaxies. *ApJ*, 854, 2 (Feb. 2018), 110. doi:10.3847/1538-4357/aaa8e4. (cited on page 13)
- ZHANG, D.; THOMPSON, T. A.; QUATAERT, E.; AND MURRAY, N., 2017. Entrainment in trouble: cool cloud acceleration and destruction in hot supernova-driven galactic winds. *MNRAS*, 468, 4 (Jul. 2017), 4801–4814. doi:10.1093/mnras/stx822. (cited on pages 3 and 35)